SIAM J. SCI. COMPUT.
Vol. 43, No. 4, pp. A2923–A2948

NUMERICAL MODELING OF THE FLUID-POROHYPERELASTIC STRUCTURE INTERACTION*

ANYASTASSIA SEBOLDT†, OYEKOLA OYEKOLE‡, JOSIP TAMBAČA§, AND MARTINA BUKAČ¶

Abstract. We consider a moving domain, fluid-porohyperelastic structure interaction problem in a dual-mixed formulation. The fluid is described using the Navier–Stokes equations, and the porohyperelastic structure is described using the Biot equations. To solve this problem numerically, we propose two novel, partitioned, loosely coupled methods based on the generalized Robin boundary conditions. In the first partitioned method, the Navier–Stokes problem is solved separately from the Biot problem. In the second proposed method, the problem is further split by separating the Biot problem into a mechanics subproblem and a Darcy subproblem. We derive the energy estimates for the proposed methods on a simplified, linear problem and show that the first partitioned method is unconditionally stable. The second partitioned method is shown to be energy-stable if the structure is viscoelastic and if certain conditions on the problem parameters and the time step are satisfied. The performance of both methods is investigated in the numerical examples.

Key words. poroelasticity, hyperelastic structure, fluid-porohyperelastic structure interaction, moving domain problem, partitioned numerical methods

AMS subject classifications. 65M12, 65M22, 76S05

DOI. 10.1137/20M1386268

1. Introduction.

Poroelastic materials are found throughout our entire universe, from large asteroids circling our galaxy to the smallest clumps of tissue inside an animal. They include both manmade and natural materials, with examples including biological systems found in bones, flesh, tissue, or blood clots; geological landscapes composed of rocks, soil, sand, or volcanic debris; and manmade substances such as ceramics, foams, or cements. To describe poroelastic structures, a commonly used model is the Biot model [7, 27], which consists of the mechanics equation describing the elastic phase and Darcy's law describing the fluid phase. The two phases are mutually coupled. In many instances, the poroelastic materials are in contact with a free-flowing fluid, and their interaction forms a two-way coupled problem. Due to their many applications, the development of numerical methods for fluid-poroelastic structure interaction (FPSI) has been an area of active research.

The enforcement of coupling conditions between the fluid and a poroelastic structure in the development of numerical methods generally varies based on which formulation is used for Darcy's equations. The primal and primal-mixed formulations allow for the natural enforcement of coupling conditions, which has been used in the design of many splitting strategies [24, 8]. This contrasts with the dual-mixed formulation,

*Submitted to the journal's Methods and Algorithms for Scientific Computing section December 15, 2020; accepted for publication (in revised form) June 1, 2021; published electronically August 19, 2021.

https://doi.org/10.1137/20M1386268

Funding: The work of the fourth author was supported by the NSF through grants DMS-1912908 and DCSD 1934300.

†Department of Applied and Computational Mathematics and Statistics, University of Notre Dame, South Bend, IN 46556 USA (aseboldt@nd.edu).

‡Department of Biomedical Engineering, The Pennsylvania State University, PA 16802 USA (kola@psu.edu).

§Department of Mathematics, University of Zagreb, Croatia (tambaca@math.hr).

¶Corresponding author. Department of Applied and Computational Mathematics and Statistics, University of Notre Dame, South Bend, IN 46556 USA (mbukac@nd.edu).

which yields a more accurate approximation to the Darcy velocity, where the kinematic coupling condition is often numerically imposed using Lagrange multipliers or penalties, commonly used in monolithic solvers [2, 29]. While the coupling is treated implicitly in monolithic methods, this approach often leads to ill-conditioned and large algebraic systems that need specifically designed preconditioners in order to converge. Although stability is easily maintained, solving a system of equations using a monolithic method can be quite computationally expensive, especially when moving domain FPSI problems with nonlinear poroelastic models are considered. Separating the problem into smaller subproblems helps to reduce the computational cost and allows the use of existing solvers. However, stability issues may arise if the partitioning is not carefully performed.

Monolithic methods for FPSI have been studied in [20, 29, 4, 2, 11, 25, 9]. In [9], a monolithic solver based on Nitsche's penalty method was presented and analyzed, and this solves was used in [29] to investigate the energy distribution of a coupled blood flow and arterial deformation. A fluid-porohyperelastic structure interaction problem was used in a computational study [20] to model the interaction between blood flow and a deformable arterial wall. In [4], a monolithic solver with incomplete LU factorization with thresholding preconditioning techniques was applied to study a coupled Navier–Stokes/Biot system. A Brinkman–Biot coupled problem was used in [11] to formulate a dimensional model reduction for flow in fractures. Monolithic solvers based on the Lagrange multiplier method were introduced and analyzed in [2, 22]. In [25], a finite element-based immersed method for an FPSI problem was introduced and used to model cell-tissue interactions. We also mention [1], where a nonlinear Stokes–Biot model for the interaction of a non-Newtonian fluid with poroelastic media was presented and analyzed.

The design of partitioned methods for FPSI is often based on extending existing partitioned methods for Stokes–Darcy interaction and fluid-structure interaction problems. Strongly coupled partitioned methods for FPSI problems based on generalized Robin boundary conditions were proposed in [4]. This approach uses a dual-mixed formulation for the Darcy's law but requires subiterations between the fluid and the Biot subproblems. Partitioned, loosely coupled methods for the interaction between a fluid, elastic structure and a poroelastic material in the primal formulation have been proposed and analyzed in [8, 10]. Two second-order accurate, loosely coupled partitioned methods for fluid-poroviscoelastic structure interaction problems were developed in [24], where their stability properties were investigated. A noniterative partitioned approach for the dual-mixed problem based on Nitsche's coupling was considered in [9]. The error analysis of this method, however, showed a reduction of accuracy due to the splitting. The partitioned scheme was then used as a preconditioner for the monolithic solver. A similar approach based on Nitsche's method was applied to a moving domain fluid-porohyperelastic structure interaction problem in [30], where the coupled problem consisting of a free fluid flow, porous media flow, and solid mechanics was split among its components and solved using a partitioned approach. We note that besides [30, 4], all of the partitioned schemes mentioned above use the assumption that the domain remains fixed.

In this work, we present novel partitioned methods for the interaction between a free-flowing fluid and a porohyperelastic structure. To model the free-flowing fluid, we use the Navier–Stokes equations in the arbitrary Lagrangian Eulerian (ALE) formulation [19, 15, 23]. The porohyperelastic structure is modeled using the Biot equations of poroelasticity in a dual-mixed formulation, and a hyperelastic structural model, allowing large deformations, is used to describe the structural mechanics. Therefore, we

formulate a dual-mixed, moving domain fluid-porohyperelastic structure interaction problem and propose two partitioned numerical methods. In the first method, the Navier–Stokes equations are solved separately from Biot's system. In the second method, the Biot problem is further split into a mechanics problem and Darcy's problem. In that way, we can first solve the mechanics problem in the Lagrangian formulation. After that, the domain is updated and the remaining flow problems are solved with respect to the current configuration. This approach also facilitates the use of Newton's method for nonlinear structural models, since only the mechanics subproblem needs to be subiterated.

The proposed methods are based on the generalized Robin interface conditions, which are formulated differently than in [4], due to which the proposed methods do not require subiterations between subproblems to achieve stability. The stability properties of the proposed methods are analyzed on a simplified, linear model. Our proof, based on energy estimates, shows that the proposed numerical method, where the problem is split into a fluid and a poroelastic material subproblem, is unconditionally stable. The second numerical scheme, where the poroelastic material is further split into a mechanics and the Darcy subproblem, is stable if the structure is poroviscoelastic and conditions on the parameters of the problem and the time step are satisfied. Both algorithms are implemented using the finite element method and investigated numerically in two examples. In the first example, we compute the convergence rates and propose a strategy for a dynamical update of the combination parameter used in the derivation of the generalized Robin boundary conditions. In the second example, we investigate the effects of the fixed domain and linear structural model assumptions on the solution using a linear structural model and a neo-Hookean model. Despite the theoretical results obtained in the stability analysis, we do not observe any instabilities in the numerical examples even when purely (hyper)elastic structure models are used.

While the partitioned methods based on Robin boundary conditions have been widely used in fluid-structure interaction problems, they have not been as widely studied in coupled flow-porous medium problems. Only a few works investigated numerical methods based on this approach, but the resulting methods required subiterations [4, 14]. To the best of our knowledge, this is the first work where the generalized Robin conditions are used to derive a partitioned, loosely coupled method, allowing us to use a mixed formulation of the Biot equations and therefore achieve better accuracy in the approximation of the Darcy velocity.

This paper is organized as follows. The mathematical model is presented in section 2. Section 3 presents the derivation of the partitioned numerical methods, which we then analyze for stability in section 4. The numerical examples are featured in section 5. Finally, conclusions are drawn in section 6.

2. Mathematical model.

2.1. Computational domains and mappings. We consider the interaction between an incompressible, Newtonian fluid and a fully saturated, deformable porous medium. We denote the reference fluid domain by $\hat{\Omega}_F$, the reference solid domain by $\hat{\Omega}_P$, and their common interface by $\hat{\Gamma}$; see Figure 1. The fluid and solid reference external boundaries are denoted by $\hat{\Sigma}_F^D \cup \hat{\Sigma}_F^N$ and $\hat{\Sigma}_P^D \cup \hat{\Sigma}_P^N$, respectively, i.e., $\partial\hat{\Omega}_F = \hat{\Sigma}_F^D \cup \hat{\Sigma}_F^N \cup \hat{\Gamma}$ and $\partial\hat{\Omega}_P = \hat{\Sigma}_P^D \cup \hat{\Sigma}_P^N \cup \hat{\Gamma}$, where subscript F refers to the fluid region and subscript P refers to the poroelastic region. The fluid and solid domains at time t are denoted by $\Omega_F(t)$ and $\Omega_P(t)$, respectively, while the interface at time t is denoted by $\Gamma(t)$. We assume that both regions are regular, bounded domains in $d = 2, 3$ dimensions.

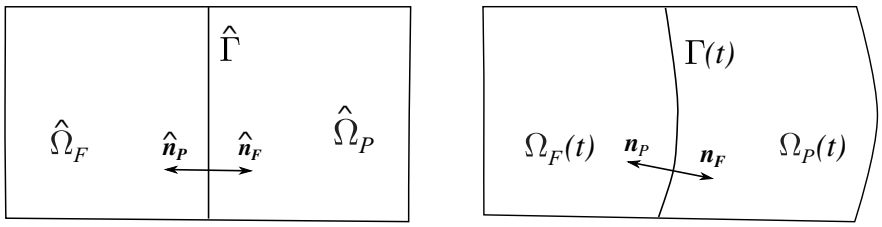

FIG. 1. *Left: Reference domains* $\hat{\Omega}_F \cup \hat{\Omega}_P$. *Right: Deformed domains* $\Omega_F(t) \cup \Omega_P(t)$.

We assume that the solid equations are given in the Lagrangian framework with respect to the reference domain $\hat{\Omega}_P$. Let the solid domain deformation be a smooth, injective mapping $\hat{\boldsymbol{\varphi}}_P : \hat{\Omega}_P \times [0,T] \to \Omega_P(t)$ from the reference to the deformed configuration given by

$$\hat{\boldsymbol{\varphi}}_P(\hat{\boldsymbol{x}},t) = \hat{\boldsymbol{x}} + \hat{\boldsymbol{\eta}}(\hat{\boldsymbol{x}},t) \quad \text{for all } \hat{\boldsymbol{x}} \in \hat{\Omega}_P, t \in [0,T],$$

where $\hat{\boldsymbol{\eta}} = (\hat{\eta}_i)_{i=1,\dots,d}$ denotes the structure displacement. The deformation gradient is given by $\hat{\boldsymbol{F}}(\hat{x},t) = \hat{\nabla}\hat{\boldsymbol{\varphi}}_P(\hat{x},t) = \boldsymbol{I} + \hat{\nabla}\hat{\boldsymbol{\eta}}(\hat{x},t)$, and its determinant is denoted by $\hat{J}$.

To track the deformation of the fluid domain in time, we introduce a smooth, invertible, ALE mapping $\hat{\boldsymbol{\varphi}}_F : \hat{\Omega}_F \times [0,T] \to \Omega_F(t)$ given by

$$\hat{\boldsymbol{\varphi}}_F(\hat{\boldsymbol{x}},t) = \hat{\boldsymbol{x}} + \hat{\boldsymbol{\eta}}_F(\hat{\boldsymbol{x}},t) \quad \text{for all } \hat{\boldsymbol{x}} \in \hat{\Omega}_F, t \in [0,T],$$

where $\hat{\boldsymbol{\eta}}_F$ denotes the fluid displacement. We assume that the fluid displacement equals the structure displacement, $\hat{\boldsymbol{\eta}} = \hat{\boldsymbol{\eta}}_F$, on $\hat{\Gamma}$ and is arbitrarily extended into the fluid domain $\hat{\Omega}_F$ [15]. We denote the determinant of $\hat{\boldsymbol{\varphi}}_F$ by $\hat{J}_F$. For any function $f : \Omega_F(t) \times [0,T] \to \mathbb{R}$, we indicate with $\hat{f} = f \circ \hat{\boldsymbol{\varphi}}_F$ the corresponding function in the ALE frame:

$$\hat{f} : \hat{\Omega}_F \times [0,T] \to \mathbb{R}, \quad \hat{f}(\hat{\boldsymbol{x}},t) = f(\hat{\boldsymbol{\varphi}}_F(\hat{\boldsymbol{x}},t),t). \tag{2.1}$$

2.2. Fluid subproblem. We use the Navier–Stokes equations in the ALE formulation to describe the fluid flow. The ALE time derivative of a function $\boldsymbol{u}$ is defined to be the Eulerian description of the ALE field $\partial_t \hat{\boldsymbol{u}}$ [16], i.e., $\partial_t \boldsymbol{u}|_{\hat{\Omega}_F} = \partial_t \hat{\boldsymbol{u}} \circ \hat{\boldsymbol{\varphi}}_F^{-1}$. Then, the following identity holds:

$$\partial_t \boldsymbol{u}|_{\hat{\Omega}_F} = \boldsymbol{w} \cdot \nabla \boldsymbol{u} + \partial_t \boldsymbol{u},$$

where $\boldsymbol{w}$ is the domain velocity given by $\boldsymbol{w} = \partial_t \boldsymbol{x}|_{\hat{\Omega}_F} = \partial_t \hat{\boldsymbol{\varphi}}_F \circ \hat{\boldsymbol{\varphi}}_F^{-1}$.

The fluid problem in the ALE form is given by

$$\rho_F \left(\partial_t \boldsymbol{v}|_{\hat{\Omega}_F} + (\boldsymbol{v} - \boldsymbol{w}) \cdot \nabla \boldsymbol{v} \right) = \nabla \cdot \boldsymbol{\sigma}_F(\boldsymbol{v}, p_F) + \boldsymbol{f} \qquad \text{in } \Omega_F(t) \times (0,T), \tag{2.2a}$$

$$\nabla \cdot \boldsymbol{v} = 0 \qquad \text{in } \Omega_F(t) \times (0,T), \tag{2.2b}$$

$$\boldsymbol{\sigma}_F \boldsymbol{n}_F = \boldsymbol{g} \qquad \text{on } \Sigma_F^N(t) \times (0,T), \tag{2.2c}$$

$$\boldsymbol{v} = \boldsymbol{0} \qquad \text{on } \Sigma_F^D(t) \times (0,T), \tag{2.2d}$$

where $\boldsymbol{v}$ is the fluid velocity, $\boldsymbol{w}$ is the domain velocity, ρ_F is the fluid density, $\boldsymbol{n}_F$ is the outward normal vector, $\boldsymbol{\sigma}_F$ is the fluid stress, tensor, and $\boldsymbol{f}$ and $\boldsymbol{g}$ are the forcing terms. For a Newtonian fluid, the stress tensor is given by $\boldsymbol{\sigma}_F(\boldsymbol{v}, p_F) = -p_F \boldsymbol{I} +$

$2\mu_F \boldsymbol{D}(\boldsymbol{v})$, where p_F is the fluid pressure, μ_F is the fluid viscosity, and $\boldsymbol{D}(\boldsymbol{v}) = (\nabla \boldsymbol{v} + (\nabla \boldsymbol{v})^T)/2$ is the strain rate tensor.

We note that the ALE method works well for small to moderate deformations. For examples with large changes in the domain, a different approach may have to be considered, such as combining the ALE with remeshing or, for example, using a hybrid ALE method presented in [5].

2.3. Biot subproblem. To describe the deformation of the solid, we use Biot's poroelasticity equations, whose formulation in the Lagrangian framework is given by [30, 7, 13, 27]:

$$\hat{\rho}_P \partial_t \hat{\boldsymbol{\xi}} = \hat{\nabla} \cdot \left(\hat{\boldsymbol{F}} \hat{\boldsymbol{S}}^P \right) \qquad \text{in } \hat{\Omega}_P \times (0,T), \tag{2.3a}$$

$$\hat{\boldsymbol{\kappa}}^{-1} \hat{\boldsymbol{q}} = -\hat{\nabla} \hat{p}_P \qquad \text{in } \hat{\Omega}_P \times (0,T), \tag{2.3b}$$

$$c_0 \partial_t \hat{p}_P + \alpha \hat{J} (\hat{\boldsymbol{F}}^{-T} \hat{\nabla}) \cdot \hat{\boldsymbol{\xi}} + \hat{\nabla} \cdot \hat{\boldsymbol{q}} = 0 \qquad \text{in } \hat{\Omega}_P \times (0,T), \tag{2.3c}$$

$$\hat{\boldsymbol{F}} \hat{\boldsymbol{S}}^P \hat{\boldsymbol{n}}_P = \boldsymbol{0},\ p_P = 0 \qquad \text{on } \hat{\Sigma}_P^N \times (0,T), \tag{2.3d}$$

$$\hat{\boldsymbol{\eta}} = \boldsymbol{0},\ \hat{\boldsymbol{q}} \cdot \hat{\boldsymbol{n}}_P = 0 \qquad \text{on } \hat{\Sigma}_P^D \times (0,T), \tag{2.3e}$$

where $\hat{p}_P$ is the fluid pore pressure, $\hat{\boldsymbol{\xi}} = \partial_t \hat{\boldsymbol{\eta}}$ is the solid velocity, $\hat{\boldsymbol{q}}$ is the average velocity of the fluid relative to the velocity of the solid, $\hat{\rho}_P$ is the density of the solid material, $\hat{\boldsymbol{\kappa}}$ is the hydraulic conductivity tensor, $\hat{c}_0$ is the storativity coefficient, and α is the Biot–Willis parameter accounting for the coupling strength between the fluid and solid phases. The second Piola–Kirchhoff stress tensor for the poroelastic structure is $\hat{\boldsymbol{S}}^P = \hat{\boldsymbol{S}} - \alpha \hat{J} \hat{p}_P \hat{\boldsymbol{C}}^{-1}$, where $\hat{\boldsymbol{S}}$ is the second Piola–Kirchhoff stress for the elastic phase and $\hat{\boldsymbol{C}} = \hat{\boldsymbol{F}}^T \hat{\boldsymbol{F}}$ is the right Cauchy–Green deformation tensor. We assume that the structure is governed by a hyperelastic model, in which case $\hat{\boldsymbol{S}} = 2\frac{\partial \hat{\boldsymbol{W}}}{\partial \hat{\boldsymbol{C}}}$, where $\hat{\boldsymbol{W}}$ is the strain energy density function. The particular choices of $\hat{\boldsymbol{W}}$ will be specified in section 5. The Cauchy stress tensor for the poroelastic structure is given by

$$\boldsymbol{\sigma}_P = \hat{J}^{-1} \hat{\boldsymbol{F}} \hat{\boldsymbol{S}}^P \hat{\boldsymbol{F}}^T.$$

The fluid pore pressure, $\hat{p}_P$, solid velocity, $\hat{\boldsymbol{\xi}}$, and displacement, $\hat{\boldsymbol{\eta}}$, in the reference configuration are related to their Eulerian counterparts via $\hat{p}_P = p_P \circ \hat{\boldsymbol{\varphi}}_P, \hat{\boldsymbol{\xi}} = \boldsymbol{\xi} \circ \hat{\boldsymbol{\varphi}}_P$, and $\hat{\boldsymbol{\eta}} = \boldsymbol{\eta} \circ \hat{\boldsymbol{\varphi}}_P$, while the Darcy velocity and the hydraulic conductivity tensor are related through the Piola transform, given by [27]

$$\hat{\boldsymbol{q}} = \hat{J} \hat{\boldsymbol{F}}^{-1} \boldsymbol{q}, \quad \hat{\boldsymbol{\kappa}} = \hat{J} \hat{\boldsymbol{F}}^{-1} \boldsymbol{\kappa} \hat{\boldsymbol{F}}^{-T}. \tag{2.4}$$

2.4. Coupling conditions. To couple the fluid and poroelastic material, we follow the approach in [28, 6]. The fluid mass conservation across the interface is given by

$$(\boldsymbol{\xi} + \boldsymbol{q}) \cdot \boldsymbol{n}_F = \boldsymbol{v} \cdot \boldsymbol{n}_F \quad \text{on } \Gamma(t) \times (0,T). \tag{2.5}$$

We assume that the Darcy flow across the interface is driven by the jump between the normal fluid stress and the pressure internal to the porous medium according to

$$\boldsymbol{n}_F \cdot \boldsymbol{\sigma}_F \boldsymbol{n}_F + p_P = \delta \boldsymbol{q} \cdot \boldsymbol{n}_P \quad \text{on } \Gamma(t) \times (0,T), \tag{2.6}$$

where $\delta \geq 0$ is the fluid entry resistance. To prescribe the conservation of momentum, we impose

$$\boldsymbol{\sigma}_F \boldsymbol{n}_F = \boldsymbol{\sigma}_P \boldsymbol{n}_F \qquad \text{on } \Gamma(t) \times (0,T). \tag{2.7}$$

Finally, we prescribe the Beavers–Joseph–Saffman condition with slip rate $\gamma > 0$, given by

$$\boldsymbol{\tau}_{F,i} \cdot \boldsymbol{\sigma}_F \boldsymbol{n}_F = -\gamma(\boldsymbol{v} - \boldsymbol{\xi}) \cdot \boldsymbol{\tau}_{F,i} \quad \text{for } i = 1, \dots, d-1 \quad \text{on } \Gamma(t) \times (0,T), \tag{2.8}$$

where $\boldsymbol{\tau}_{F,i} = \boldsymbol{\tau}_{P,i}$, $i = 1, \dots, d-1$, is the orthonormal basis for the tangential space of $\Gamma(t)$.

2.5. Weak formulation and energy estimates of the continuous problem. Given an open set S, we consider the usual Sobolev spaces $H^k(S)$ with $k \geq 0$. For all $t \in [0,T]$, we introduce the following functional spaces:

$$V^F(t) = \left\{ \boldsymbol{\phi} : \Omega_F(t) \to \mathbb{R}^d \mid \boldsymbol{\phi} = \hat{\boldsymbol{\phi}} \circ \boldsymbol{\varphi}_F^{-1},\ \hat{\boldsymbol{\phi}} \in (H^1(\hat{\Omega}_F))^d, \hat{\boldsymbol{\phi}} = \mathbf{0} \text{ on } \hat{\Sigma}_F^D \right\},$$

$$X^F(t) = \left\{ \psi : \Omega_F(t) \to \mathbb{R} \mid \psi = \hat{\psi} \circ \boldsymbol{\varphi}_F^{-1},\ \hat{\psi} \in L^2(\hat{\Omega}_F) \right\},$$

$$\hat{V}^P = \left\{ \hat{\boldsymbol{\zeta}} : \hat{\Omega}_P \to \mathbb{R}^d \mid \hat{\boldsymbol{\zeta}} \in (H^1(\hat{\Omega}_P))^d,\ \hat{\boldsymbol{\zeta}} = \mathbf{0} \text{ on } \hat{\Sigma}_P^D \right\},$$

$$V^P(t) = \left\{ \boldsymbol{\zeta} : \Omega_P(t) \to \mathbb{R}^d \mid \boldsymbol{\zeta} = \hat{\boldsymbol{\zeta}} \circ \boldsymbol{\varphi}_P^{-1},\ \hat{\boldsymbol{\zeta}} \in \hat{V}^P \right\},$$

$$\hat{V}^Q = \left\{ \hat{\boldsymbol{r}} : \hat{\Omega}_P \to \mathbb{R}^d \mid \hat{\nabla} \cdot \hat{\boldsymbol{r}} \in L^2(\hat{\Omega}_P),\ \hat{\boldsymbol{r}} \cdot \hat{\boldsymbol{n}}_P = 0 \text{ on } \hat{\Sigma}_P^D \right\},$$

$$V^Q(t) = \left\{ \boldsymbol{r} : \Omega_P(t) \to \mathbb{R}^d \mid \boldsymbol{r} = \hat{J}^{-1} \hat{\boldsymbol{F}} \hat{\boldsymbol{r}},\ \hat{\boldsymbol{r}} \in \hat{V}^Q \right\},$$

$$\hat{X}^P = \left\{ \hat{\psi} : \hat{\Omega}_P \to \mathbb{R} \mid \hat{\psi} \in L^2(\hat{\Omega}_P) \right\}, \quad X^P(t) = \left\{ \psi : \Omega_P(t) \to \mathbb{R} \mid \psi = \hat{\psi} \circ \boldsymbol{\varphi}_P^{-1},\ \hat{\psi} \in \hat{X}^P \right\},$$

$$V^{NSB}(t) = \left\{ (\boldsymbol{\phi}, \boldsymbol{\zeta}, \boldsymbol{r}) \in V^F(t) \times V^P(t) \times V^Q(t) \mid \boldsymbol{\phi} \cdot \boldsymbol{n}_F = (\boldsymbol{\zeta} + \boldsymbol{r}) \cdot \boldsymbol{n}_F \text{ on } \Gamma(t) \right\}.$$

We define the following bilinear forms associated with the fluid problem:

$$a_F^t(\boldsymbol{v}, \boldsymbol{\phi}) = 2\mu \int_{\Omega_F(t)} \boldsymbol{D}(\boldsymbol{v}) : \boldsymbol{D}(\boldsymbol{\phi}) d\boldsymbol{x}, \qquad b_F^t(p, \boldsymbol{\phi}) = \int_{\Omega_F(t)} p \nabla \cdot \boldsymbol{\phi} d\boldsymbol{x}$$

for all $\boldsymbol{v}, \boldsymbol{\phi} \in V^F(t)$ and $p \in X^F(t)$. To shorten the notation, we introduce

$$a_S(\hat{\boldsymbol{\eta}}, \hat{\boldsymbol{\zeta}}) = \int_{\hat{\Omega}_P} \hat{\boldsymbol{F}} \hat{\boldsymbol{S}}(\hat{\boldsymbol{\eta}}) : \hat{\nabla} \hat{\boldsymbol{\zeta}} d\hat{\boldsymbol{x}}, \qquad b_S(\hat{p}_P, \hat{\boldsymbol{\zeta}}) = \int_{\hat{\Omega}_P} \alpha \hat{J} \hat{p}_P \hat{\boldsymbol{F}}^{-T} : \hat{\nabla} \hat{\boldsymbol{\zeta}} d\hat{\boldsymbol{x}}$$

and consider them on a subset of $\hat{V}^P$ on which the integrals are well-defined. We also define bilinear forms associated with the Darcy problem:

$$a_Q(\hat{\boldsymbol{q}}, \hat{\boldsymbol{r}}) = \int_{\hat{\Omega}_P} \hat{\boldsymbol{\kappa}}^{-1} \hat{\boldsymbol{q}} \cdot \hat{\boldsymbol{r}} d\hat{\boldsymbol{x}}, \qquad b_Q(\hat{p}_P, \hat{\boldsymbol{r}}) = \int_{\hat{\Omega}_P} \hat{p}_P \hat{\nabla} \cdot \hat{\boldsymbol{r}} d\hat{\boldsymbol{x}}$$

for all $\hat{\boldsymbol{q}}, \hat{\boldsymbol{r}} \in \hat{V}^Q$ and $\hat{p}_P \in \hat{X}^P$ and

$$a_Q^t(\boldsymbol{q}, \boldsymbol{r}) = \int_{\Omega_P(t)} \boldsymbol{\kappa}^{-1} \boldsymbol{q} \cdot \boldsymbol{r} d\boldsymbol{x}, \qquad b_Q^t(p_P, \boldsymbol{r}) = \int_{\Omega_P(t)} p_P \nabla \cdot \boldsymbol{r} d\boldsymbol{x}$$

for all $\boldsymbol{q}, \boldsymbol{r} \in V^Q$ and $p_P \in X^P$.

To derive the weak formulation, we multiply the fluid problem (2.2a)–(2.2b) by $\boldsymbol{\phi}$ and ψ, respectively, the structure problem (2.3a)–(2.3c) by $\hat{\boldsymbol{\zeta}}, \hat{\boldsymbol{r}}$ and $\hat{\varphi}$, respectively, and add the equations together, obtaining

(2.9)

$$\begin{aligned}
&\rho_F \int_{\Omega_F(t)} \partial_t \boldsymbol{v}|_{\hat{\Omega}_F} \cdot \boldsymbol{\phi} d\boldsymbol{x} + \rho_F \int_{\Omega_F(t)} ((\boldsymbol{v}-\boldsymbol{w})\cdot\nabla)\,\boldsymbol{v}\cdot\boldsymbol{\phi} d\boldsymbol{x} + a_F^t(\boldsymbol{v},\boldsymbol{\phi}) - b_F^t(p_F,\boldsymbol{\phi}) + b_F^t(\psi,\boldsymbol{v}) \\
&\quad + \hat{\rho}_P \int_{\hat{\Omega}_P} \partial_t \hat{\boldsymbol{\xi}}\cdot\hat{\boldsymbol{\zeta}} d\hat{\boldsymbol{x}} + a_S(\hat{\boldsymbol{\eta}},\hat{\boldsymbol{\zeta}}) - b_S(\hat{p}_P,\hat{\boldsymbol{\zeta}}) + a_Q(\hat{\boldsymbol{q}},\hat{\boldsymbol{r}}) - b_Q(\hat{p}_P,\hat{\boldsymbol{r}}) \\
&\quad + c_0 \int_{\hat{\Omega}_P} \partial_t \hat{p}_P \hat{\varphi} + b_S(\hat{\varphi},\hat{\boldsymbol{\xi}}) + b_Q(\hat{\varphi},\hat{\boldsymbol{q}}) \\
&= \underbrace{\int_{\Gamma(t)} \boldsymbol{\sigma}_F \boldsymbol{n}_F\cdot\boldsymbol{\phi} dx + \int_{\hat{\Gamma}} \hat{\boldsymbol{F}}\hat{\boldsymbol{S}}^P\hat{\boldsymbol{n}}_P\cdot\hat{\boldsymbol{\zeta}} d\hat{x} - \int_{\hat{\Gamma}} \hat{p}_P\hat{\boldsymbol{r}}\cdot\hat{\boldsymbol{n}}_P d\hat{\boldsymbol{x}}}_{\mathcal{I}} + \int_{\Omega_F(t)} \boldsymbol{f}_F\cdot\boldsymbol{\phi} d\boldsymbol{x} + \int_{\Sigma_F^N(t)} \boldsymbol{g}\cdot\boldsymbol{\phi} dx,
\end{aligned}$$

for all $\boldsymbol{\phi} \in V^F(t), \psi \in X^F(t), \hat{\boldsymbol{\zeta}} \in \hat{V}^P, \hat{\boldsymbol{r}} \in \hat{V}^Q, \hat{\varphi} \in X^P$. Recasting the solid interface terms to $\Gamma(t)$, decomposing the stresses into normal and tangential components, and using (2.5)–(2.8) we have

$$\begin{aligned}
\mathcal{I} &= \int_{\Gamma(t)} (\boldsymbol{n}_F\cdot\boldsymbol{\sigma}_F\boldsymbol{n}_F)(\boldsymbol{\phi}\cdot\boldsymbol{n}_F) dx + \sum_{i=1}^{d-1} \int_{\Gamma(t)} (\boldsymbol{\tau}_{F,i}\cdot\boldsymbol{\sigma}_F\boldsymbol{n}_F)(\boldsymbol{\phi}\cdot\boldsymbol{\tau}_{F,i}) dx - \int_{\Gamma(t)} p_P\boldsymbol{r}\cdot\boldsymbol{n}_P d\boldsymbol{x} \\
&\quad + \int_{\Gamma(t)} (\boldsymbol{n}_P\cdot\boldsymbol{\sigma}_P\boldsymbol{n}_P)(\boldsymbol{\zeta}\cdot\boldsymbol{n}_P) dx + \sum_{i=1}^{d-1} \int_{\Gamma(t)} (\boldsymbol{\tau}_{P,i}\cdot\boldsymbol{\sigma}_P\boldsymbol{n}_P)(\boldsymbol{\zeta}\cdot\boldsymbol{\tau}_{P,i}) dx \\
&= \int_{\Gamma(t)} (\delta\boldsymbol{q}\cdot\boldsymbol{n}_P - p_P)\,(\boldsymbol{\phi}-\boldsymbol{\zeta})\cdot\boldsymbol{n}_F dx - \sum_{i=1}^{d-1} \int_{\Gamma(t)} \gamma(\boldsymbol{v}-\boldsymbol{\xi})\cdot\boldsymbol{\tau}_{F,i}(\boldsymbol{\phi}-\boldsymbol{\zeta})\cdot\boldsymbol{\tau}_{F,i} dx \\
&\quad - \int_{\Gamma(t)} p_P\boldsymbol{r}\cdot\boldsymbol{n}_P d\boldsymbol{x}.
\end{aligned}$$

Grouping similar terms and assuming that $(\boldsymbol{\phi},\boldsymbol{\zeta},\boldsymbol{r}) \in V^{NSB}(t)$, we get

$$\mathcal{I} = -\int_{\Gamma(t)} \delta(\boldsymbol{q}\cdot\boldsymbol{n}_P)(\boldsymbol{r}\cdot\boldsymbol{n}_P) dx - \int_{\Gamma(t)} \sum_{i=1}^{d-1} \gamma(\boldsymbol{v}-\boldsymbol{\xi})\cdot\boldsymbol{\tau}_{F,i}(\boldsymbol{\phi}-\boldsymbol{\zeta})\cdot\boldsymbol{\tau}_{F,i} dx. \tag{2.10}$$

Combining (2.10) with (2.9), we get the following weak formulation: Find $(\boldsymbol{v},\boldsymbol{\xi},\boldsymbol{q}) \in V^{NSB}(t), p_F \in X^F(t)$ and $\hat{p}_P \in X^P$, where $\hat{\boldsymbol{\xi}} = \boldsymbol{\xi}\circ\boldsymbol{\varphi}_P, \hat{\boldsymbol{q}} = \hat{J}\hat{\boldsymbol{F}}^{-1}\boldsymbol{q}$ and $\hat{\boldsymbol{\xi}} = \partial_t\hat{\boldsymbol{\eta}}$, such that

$$\begin{aligned}
&\rho_F \int_{\Omega_F(t)} \partial_t \boldsymbol{v}|_{\hat{\Omega}_F} \cdot \boldsymbol{\phi} d\boldsymbol{x} + \rho_F \int_{\Omega_F(t)} ((\boldsymbol{v}-\boldsymbol{w})\cdot\nabla)\,\boldsymbol{v}\cdot\boldsymbol{\phi} d\boldsymbol{x} + a_F^t(\boldsymbol{v},\boldsymbol{\phi}) - b_F^t(p_F,\boldsymbol{\phi}) + b_F^t(\psi,\boldsymbol{v}) \\
&\quad + \hat{\rho}_P \int_{\hat{\Omega}_P} \partial_t \hat{\boldsymbol{\xi}}\cdot\hat{\boldsymbol{\zeta}} d\hat{\boldsymbol{x}} + a_S(\hat{\boldsymbol{\eta}},\hat{\boldsymbol{\zeta}}) - b_S(\hat{p}_P,\hat{\boldsymbol{\zeta}}) + a_Q(\hat{\boldsymbol{q}},\hat{\boldsymbol{r}}) - b_Q(\hat{p}_P,\hat{\boldsymbol{r}}) + c_0 \int_{\hat{\Omega}_P} \partial_t \hat{p}_P \hat{\varphi} + b_S(\hat{\varphi},\hat{\boldsymbol{\xi}}) \\
&\quad + b_Q(\hat{\varphi},\hat{\boldsymbol{q}}) + \int_{\Gamma(t)} \delta(\boldsymbol{q}\cdot\boldsymbol{n}_P)(\boldsymbol{r}\cdot\boldsymbol{n}_P) dx + \int_{\Gamma(t)} \sum_{i=1}^{d-1} \gamma(\boldsymbol{v}-\boldsymbol{\xi})\cdot\boldsymbol{\tau}_{F,i}(\boldsymbol{\phi}-\boldsymbol{\zeta})\cdot\boldsymbol{\tau}_{F,i} dx \\
&= \int_{\Omega_F(t)} \boldsymbol{f}_F\cdot\boldsymbol{\phi} d\boldsymbol{x} + \int_{\Sigma_F^N(t)} \boldsymbol{g}\cdot\boldsymbol{\phi} dx,
\end{aligned}$$

for all $(\boldsymbol{\phi},\boldsymbol{\zeta},\boldsymbol{r}) \in V^{NSB}(t), \psi \in X^F(t), \hat{\varphi} \in X^P$.

3. Numerical scheme. Let Δt denote the time step and $t^n = n\Delta t$ for $n = 0,\ldots,N$, where $T = N\Delta t$ is the final time. In the following, we will denote the discrete time derivative of a function $\boldsymbol{u}$ at time t^{n+1} by $d_t\boldsymbol{u}^{n+1}$, defined as

$$d_t\boldsymbol{u}^{n+1} = \frac{\boldsymbol{u}^{n+1}-\boldsymbol{u}^n}{\Delta t}.$$

The proposed scheme is based on generalized Robin boundary conditions, which are obtained by multiplying (2.5) by a combination parameter $L \geq 0$ and adding it to $\boldsymbol{n}_F \cdot \boldsymbol{\sigma}_F \boldsymbol{n}_F$ as follows:

$$\boldsymbol{n}_F \cdot \boldsymbol{\sigma}_F \boldsymbol{n}_F + L\boldsymbol{v} \cdot \boldsymbol{n}_F = \boldsymbol{n}_F \cdot \boldsymbol{\sigma}_F \boldsymbol{n}_F + L\left(\boldsymbol{\xi} + \boldsymbol{q}\right) \cdot \boldsymbol{n}_F \quad \text{on } \Gamma(t) \times (0,T). \tag{3.1}$$

Evaluating the normal component of fluid normal stress on the left at time t^{n+1} and one on the right at t^n, we will obtain a Robin boundary condition for the fluid problem. The same condition will be used in the structure problem (2.3a) after noting that, due to (2.7), we have

$$\boldsymbol{n}_P \cdot \boldsymbol{\sigma}_P \boldsymbol{n}_P = \boldsymbol{n}_F \cdot \boldsymbol{\sigma}_F \boldsymbol{n}_F = \boldsymbol{n}_F \cdot \boldsymbol{\sigma}_F \boldsymbol{n}_F + L\left(\boldsymbol{\xi} + \boldsymbol{q} - \boldsymbol{v}\right) \cdot \boldsymbol{n}_F. \tag{3.2}$$

Noting that $\delta \boldsymbol{q} \cdot \boldsymbol{n}_P - p_P = \boldsymbol{n}_F \cdot \boldsymbol{\sigma}_F \boldsymbol{n}_F$, we can write (3.1) as

$$\boldsymbol{n}_F \cdot \boldsymbol{\sigma}_F \boldsymbol{n}_F + L\boldsymbol{v} \cdot \boldsymbol{n}_F = \delta \boldsymbol{q} \cdot \boldsymbol{n}_P - p_P + L\left(\boldsymbol{\xi} + \boldsymbol{q}\right) \cdot \boldsymbol{n}_F \quad \text{on } \Gamma(t) \times (0,T). \tag{3.3}$$

Expressing p_P from (3.3) will give us a Robin condition for the Darcy problem (2.3b). We also note that, due to (2.7), we have

$$\boldsymbol{\tau}_{P,i} \cdot \boldsymbol{\sigma}_P \boldsymbol{n}_P = \gamma(\boldsymbol{v} - \boldsymbol{\xi}) \cdot \boldsymbol{\tau}_{P,i} \quad \text{for } i = 1, \ldots, d-1 \quad \text{on } \Gamma(t) \times (0,T). \tag{3.4}$$

To derive the partitioned scheme, we start from the monolithic weak formulation (2.9). Focusing on the interface integral and decomposing the stress in the normal and tangential components, we have

$$\begin{aligned}\mathcal{I} = &\int_{\Gamma(t)} (\boldsymbol{n}_F \cdot \boldsymbol{\sigma}_F \boldsymbol{n}_F)(\boldsymbol{\phi} \cdot \boldsymbol{n}_F) dx + \sum_{i=1}^{d-1} \int_{\Gamma(t)} (\boldsymbol{\tau}_{F,i} \cdot \boldsymbol{\sigma}_F \boldsymbol{n}_F)(\boldsymbol{\phi} \cdot \boldsymbol{\tau}_{F,i}) dx - \int_{\Gamma(t)} p_P \boldsymbol{r} \cdot \boldsymbol{n}_P d\boldsymbol{x} \\ &+ \int_{\Gamma(t)} (\boldsymbol{n}_P \cdot \boldsymbol{\sigma}_P \boldsymbol{n}_P)(\boldsymbol{\zeta} \cdot \boldsymbol{n}_P) dx + \sum_{i=1}^{d-1} \int_{\Gamma(t)} (\boldsymbol{\tau}_{P,i} \cdot \boldsymbol{\sigma}_P \boldsymbol{n}_P)(\boldsymbol{\zeta} \cdot \boldsymbol{\tau}_{P,i}) dx.\end{aligned}$$

Plugging in conditions (3.1) and (2.8) in the fluid part and (3.2), (3.4), and (3.3) in the solid part, we obtain

$$\begin{aligned}\mathcal{I} = &\int_{\Gamma(t)} \left(L\left(\boldsymbol{\xi} + \boldsymbol{q} - \boldsymbol{v}\right) \cdot \boldsymbol{n}_F + \boldsymbol{n}_F \cdot \boldsymbol{\sigma}_F \boldsymbol{n}_F\right)(\boldsymbol{\phi} \cdot \boldsymbol{n}_F) dx \\ &+ \int_{\Gamma(t)} \left(-L\left(\boldsymbol{\xi} + \boldsymbol{q} - \boldsymbol{v}\right) \cdot \boldsymbol{n}_P + \boldsymbol{n}_F \cdot \boldsymbol{\sigma}_F \boldsymbol{n}_F\right)(\boldsymbol{\zeta} \cdot \boldsymbol{n}_P) dx \\ &- \sum_{i=1}^{d-1} \int_{\Gamma(t)} \gamma(\boldsymbol{v} - \boldsymbol{\xi}) \cdot \boldsymbol{\tau}_{F,i} \boldsymbol{\phi} \cdot \boldsymbol{\tau}_{F,i} dx + \sum_{i=1}^{d-1} \int_{\Gamma(t)} \gamma(\boldsymbol{v} - \boldsymbol{\xi}) \cdot \boldsymbol{\tau}_{P,i} \boldsymbol{\zeta} \cdot \boldsymbol{\tau}_{P,i} dx \\ &- \int_{\Gamma(t)} (\delta \boldsymbol{q} \cdot \boldsymbol{n}_P - \boldsymbol{n}_F \cdot \boldsymbol{\sigma}_F \boldsymbol{n}_F + L\left(\boldsymbol{\xi} + \boldsymbol{q} - \boldsymbol{v}\right) \cdot \boldsymbol{n}_P)(\boldsymbol{r} \cdot \boldsymbol{n}_P) d\boldsymbol{x}.\end{aligned} \tag{3.5}$$

Note that all the coupling conditions have been taken into account. To discretize the problem in time and decouple the fluid and structure, we time-lag the fluid variables that will appear in the Biot subproblem. After solving the Biot subproblem, we take the most recent variables in the fluid problem. Furthermore, to avoid additional nonlinearities, we evaluate the interface integral in the Biot subproblem on $\Gamma(t^n)$, giving the following discrete approximation of (3.5):

$$\begin{aligned}\mathcal{I} \approx &\int_{\Gamma(t^{n+1})} \left(L\left(\boldsymbol{\xi}^{n+1} + \boldsymbol{q}^{n+1} - \boldsymbol{v}^{n+1}\right) \cdot \boldsymbol{n}_F^{n+1} + \boldsymbol{n}_F^n \cdot \boldsymbol{\sigma}_F^n \boldsymbol{n}_F^n\right)(\boldsymbol{\phi} \cdot \boldsymbol{n}_F^{n+1}) dx \\ &+ \int_{\Gamma(t^n)} \left(-L\left(\boldsymbol{\xi}^{n+1} + \boldsymbol{q}^{n+1} - \boldsymbol{v}^n\right) \cdot \boldsymbol{n}_P^n + \boldsymbol{n}_F^n \cdot \boldsymbol{\sigma}_F^n \boldsymbol{n}_F^n\right)(\boldsymbol{\zeta} \cdot \boldsymbol{n}_P^n) dx\end{aligned} \tag{3.6}$$

$$-\sum_{i=1}^{d-1}\int_{\Gamma(t^{n+1})}\gamma(\boldsymbol{v}^{n+1}-\boldsymbol{\xi}^{n+1})\cdot\boldsymbol{\tau}_{F,i}^{n+1}\boldsymbol{\phi}\cdot\boldsymbol{\tau}_{F,i}^{n+1}dx+\sum_{i=1}^{d-1}\int_{\Gamma(t^{n})}\gamma(\boldsymbol{v}^{n}-\boldsymbol{\xi}^{n+1})\cdot\boldsymbol{\tau}_{F,i}^{n}\boldsymbol{\zeta}\cdot\boldsymbol{\tau}_{F,i}^{n}dx$$
$$-\int_{\Gamma(t^{n})}\left(\delta\boldsymbol{q}^{n+1}\cdot\boldsymbol{n}_P^n-\boldsymbol{n}_F^n\cdot\boldsymbol{\sigma}_F^n\boldsymbol{n}_F^n+L\left(\boldsymbol{\xi}^{n+1}+\boldsymbol{q}^{n+1}-\boldsymbol{v}^n\right)\cdot\boldsymbol{n}_P^n\right)(\boldsymbol{r}\cdot\boldsymbol{n}_P^n)d\boldsymbol{x}.$$

To discretize the other terms in (2.9), we apply the backward Euler method. This method is chosen to discretize the structural problem because it has been shown that the second-order conservative methods, such as the trapezoidal and the midpoint rule, exhibit numerical instabilities in real-life simulations and hence do not work well for nonlinear structures [21]. The proposed semidiscretized numerical scheme in the weak form is described in Algorithm 3.1.

Algorithm 3.1. Biot–Navier–Stokes partitioned method

Given $\hat{\boldsymbol{\eta}}^0,\hat{\boldsymbol{\xi}}^0,\boldsymbol{v}^0,p_F^0$, for $n\geq 0$, compute the following:

STEP 1 (Biot subproblem). Find $\hat{\boldsymbol{\xi}}^{n+1}=d_t\hat{\boldsymbol{\eta}}^{n+1}\in\hat{V}^S,\hat{\boldsymbol{q}}^{n+1}\in\hat{V}^Q$, and $\hat{p}_P^{n+1}\in\hat{X}^P$ such that for all $\hat{\boldsymbol{\zeta}}\in\hat{V}^S$, $\hat{\boldsymbol{r}}\in\hat{V}^Q$, and $\hat{\varphi}\in\hat{X}^P$ we have

$$\begin{aligned}(3.7)\quad &\hat{\rho}_P\int_{\hat{\Omega}_P}d_t\hat{\boldsymbol{\xi}}^{n+1}\cdot\hat{\boldsymbol{\zeta}}+a_S(\hat{\boldsymbol{\eta}}^{n+1},\hat{\boldsymbol{\zeta}})-b_S(\hat{p}_P^{n+1},\hat{\boldsymbol{\zeta}})+a_Q(\hat{\boldsymbol{q}}^{n+1},\hat{\boldsymbol{r}})-b_Q(\hat{p}_P^{n+1},\hat{\boldsymbol{r}})\\&\quad+c_0\int_{\hat{\Omega}_P}d_t\hat{p}_P^{n+1}\hat{\varphi}+b_Q(\hat{\varphi},\hat{\boldsymbol{q}}^{n+1})+b_S(\hat{\varphi},\hat{\boldsymbol{\xi}}^{n+1})\\&=\int_{\Gamma(t^n)}\boldsymbol{n}_P^n\cdot\boldsymbol{\sigma}_F^n\boldsymbol{n}_P^n\left(\boldsymbol{\zeta}+\boldsymbol{r}\right)\cdot\boldsymbol{n}_P^n-\int_{\Gamma(t^n)}L\left(\boldsymbol{\xi}^{n+1}+\boldsymbol{q}^{n+1}-\boldsymbol{v}^n\right)\cdot\boldsymbol{n}_P^n\left(\boldsymbol{\zeta}+\boldsymbol{r}\right)\cdot\boldsymbol{n}_P^n\\&\quad+\sum_{i=1}^{d-1}\int_{\Gamma(t^n)}\gamma(\boldsymbol{v}^n-\boldsymbol{\xi}^{n+1})\cdot\boldsymbol{\tau}_{P,i}^n(\boldsymbol{\zeta}\cdot\boldsymbol{\tau}_{P,i}^n)-\int_{\Gamma(t^n)}\delta\boldsymbol{q}^{n+1}\cdot\boldsymbol{n}_P^n\boldsymbol{r}\cdot\boldsymbol{n}_P^n.\end{aligned}$$

STEP 2 (geometry subproblem). In this step, we compute the fluid domain displacement and domain velocity, and we move the fluid domain. For this purpose, we use a harmonic extension, defined as follows. Find $\hat{\boldsymbol{\eta}}_F^{n+1}\in\hat{V}^F$ such that $\hat{\boldsymbol{\eta}}_F^{n+1}=0$ on $\hat{\Sigma}_F^N\cup\hat{\Sigma}_F^D$, $\hat{\boldsymbol{\eta}}_F^{n+1}=\hat{\boldsymbol{\eta}}^{n+1}$ on $\hat{\Gamma}$, and

$$(3.8)\qquad\int_{\hat{\Omega}_F}\hat{\nabla}\hat{\boldsymbol{\eta}}_F^{n+1}:\hat{\nabla}\hat{\boldsymbol{\chi}}=0$$

for all $\hat{\boldsymbol{\chi}}\in P^F$. Furthermore, compute $\hat{\boldsymbol{w}}^{n+1}$ such that $\hat{\boldsymbol{w}}^{n+1}=d_t\hat{\boldsymbol{\eta}}_F^{n+1}$ in $\hat{\Omega}_F$ and update the fluid domain by setting $\Omega_F(t^{n+1})=(I+\hat{\boldsymbol{\eta}}_F^{n+1})(\hat{\Omega}_F)$.

STEP 3 (fluid subproblem). Find $\boldsymbol{v}^{n+1}\in V^F(t^{n+1})$ and $p_F^{n+1}\in X^F(t^{n+1})$ such that for all $\boldsymbol{\phi}\in V^F(t^{n+1})$ and $\psi\in X^F(t^{n+1})$ we have

(3.9)

$$\begin{aligned}&\rho_F\int_{\Omega_F(t^{n+1})}d_t\boldsymbol{v}^{n+1}\cdot\boldsymbol{\phi}+\rho_F\int_{\Omega_F(t^{n+1})}\left(\left(\boldsymbol{v}^n-\boldsymbol{w}^{n+1}\right)\cdot\nabla\right)\boldsymbol{v}^{n+1}\cdot\boldsymbol{\phi}+a_F^{n+1}(\boldsymbol{v}^{n+1},\boldsymbol{\phi})\\&\quad-b_F^{n+1}(p_F^{n+1},\boldsymbol{\phi})+b_F^{n+1}(\psi,\boldsymbol{v}^{n+1})\\&=\int_{\Omega_F(t^{n+1})}\boldsymbol{f}^{n+1}\cdot\boldsymbol{\phi}+\int_{\Sigma_F^N(t^{n+1})}\boldsymbol{g}^{n+1}\cdot\boldsymbol{\phi}-\int_{\Gamma(t^{n+1})}L\left(\boldsymbol{v}^{n+1}-\boldsymbol{\xi}^{n+1}-\boldsymbol{q}^{n+1}\right)\cdot\boldsymbol{n}_F^{n+1}\boldsymbol{\phi}\cdot\boldsymbol{n}_F^{n+1}\\&\quad+\int_{\Gamma(t^{n+1})}(\boldsymbol{n}_F^n\cdot\boldsymbol{\sigma}_F^n\boldsymbol{n}_F^n)(\boldsymbol{\phi}\cdot\boldsymbol{n}_F^{n+1})-\sum_{i=1}^{d-1}\int_{\Gamma(t^{n+1})}\gamma(\boldsymbol{v}^{n+1}-\boldsymbol{\xi}^{n+1})\cdot\boldsymbol{\tau}_{F,i}^{n+1}\boldsymbol{\phi}\cdot\boldsymbol{\tau}_{F,i}^{n+1}.\end{aligned}$$

Set $n=n+1$ and go back to Step 1.

Algorithm 3.2. Structure Darcy–Navier–Stokes partitioned method

Given $\hat{\boldsymbol{\eta}}^0, \hat{\boldsymbol{\xi}}^0, \boldsymbol{v}^0, p_F^0$, for $n \geq 0$, compute the following:

STEP 1 (structure subproblem). Find $\hat{\boldsymbol{\xi}}^{n+1} = d_t \hat{\boldsymbol{\eta}}^{n+1} \in \hat{V}^S$ such that for all $\hat{\boldsymbol{\zeta}} \in \hat{V}^S$ we have

$$
\begin{aligned}
(3.10)\quad & \hat{\rho}_P \int_{\hat{\Omega}_P} d_t \hat{\boldsymbol{\xi}}^{n+1} \cdot \hat{\boldsymbol{\zeta}} + a_S(\hat{\boldsymbol{\eta}}^{n+1}, \hat{\boldsymbol{\zeta}}) - \int_{\hat{\Omega}_P} \alpha J^n \hat{p}_P^n (\hat{\boldsymbol{F}}^n)^{-T} : \hat{\nabla} \hat{\boldsymbol{\zeta}} d\hat{\boldsymbol{x}} \\
& = \int_{\Gamma(t^n)} (\boldsymbol{n}_P^n \cdot \boldsymbol{\sigma}_F^n \boldsymbol{n}_P^n) (\boldsymbol{\zeta} \cdot \boldsymbol{n}_P^n) - \int_{\Gamma(t^n)} L \left(\boldsymbol{\xi}^{n+1} + \boldsymbol{q}^n - \boldsymbol{v}^n \right) \cdot \boldsymbol{n}_P^n (\boldsymbol{\zeta} \cdot \boldsymbol{n}_P^n) \\
& \quad + \sum_{i=1}^{d-1} \int_{\Gamma(t^n)} \gamma (\boldsymbol{v}^n - \boldsymbol{\xi}^{n+1}) \cdot \boldsymbol{\tau}_{P,i}^n (\boldsymbol{\zeta} \cdot \boldsymbol{\tau}_{P,i}^n).
\end{aligned}
$$

STEP 2 (geometry subproblem). Find $\hat{\boldsymbol{\eta}}_F^{n+1} \in \hat{V}^F$ such that $\hat{\boldsymbol{\eta}}_F^{n+1} = 0$ on $\hat{\Sigma}_F^N \cup \hat{\Sigma}_F^D$, $\hat{\boldsymbol{\eta}}_F^{n+1} = \hat{\boldsymbol{\eta}}^{n+1}$ on $\hat{\Gamma}$, and

$$
(3.11)\qquad \int_{\hat{\Omega}_F} \hat{\nabla} \hat{\boldsymbol{\eta}}_F^{n+1} : \hat{\nabla} \hat{\boldsymbol{\chi}} = 0
$$

for all $\hat{\boldsymbol{\chi}} \in P^F$. Set $\hat{\boldsymbol{w}}^{n+1} = d_t \hat{\boldsymbol{\eta}}_F^{n+1}$ and update the fluid domain by setting $\Omega_F(t^{n+1}) = (I + \hat{\boldsymbol{\eta}}_F^{n+1})(\hat{\Omega}_F)$ and the structure domain by setting $\Omega_P(t^{n+1}) = (I + \hat{\boldsymbol{\eta}}^{n+1})(\hat{\Omega}_P)$.

STEP 3 (darcy subproblem). Find $\boldsymbol{q}^{n+1} \in V^Q(t^{n+1})$ and $p_P^{n+1} \in X^P(t^{n+1})$ such that for all $\boldsymbol{r} \in V^Q(t^{n+1})$ and $\varphi \in X^P(t^{n+1})$ we have

$$
\begin{aligned}
(3.12)\quad & a_Q^{n+1}(\boldsymbol{q}^{n+1}, \boldsymbol{r}) - b_Q^{n+1}(p_P^{n+1}, \boldsymbol{r}) + c_0 \int_{\Omega_P(t^{n+1})} d_t p_P^{n+1} \varphi + b_Q^{n+1}(\varphi, \boldsymbol{q}^{n+1}) + \int_{\Omega_P(t^{n+1})} \alpha \varphi \nabla \cdot \boldsymbol{\xi}^{n+1} \\
& = \int_{\Gamma(t^{n+1})} (\boldsymbol{n}_P^n \cdot \boldsymbol{\sigma}_F^n \boldsymbol{n}_P^n) \left(\boldsymbol{r} \cdot \boldsymbol{n}_P^{n+1} \right) - \int_{\Gamma(t^{n+1})} L \left(\boldsymbol{\xi}^{n+1} + \boldsymbol{q}^{n+1} - \boldsymbol{v}^n \right) \cdot \boldsymbol{n}_P^{n+1} \left(\boldsymbol{r} \cdot \boldsymbol{n}_P^{n+1} \right) \\
& \quad - \int_{\Gamma(t^{n+1})} \delta \left(\boldsymbol{q}^{n+1} \cdot \boldsymbol{n}_P^{n+1} \right) \left(\boldsymbol{r} \cdot \boldsymbol{n}_P^{n+1} \right).
\end{aligned}
$$

STEP 4 (fluid subproblem). Find $\boldsymbol{v}^{n+1} \in V^F(t^{n+1})$ and $p_F^{n+1} \in X^F(t^{n+1})$ such that for all $\boldsymbol{\phi} \in V^F(t^{n+1})$ and $\psi \in X^F(t^{n+1})$ we have

$$
\begin{aligned}
(3.13)\quad & \rho_F \int_{\Omega_F(t^{n+1})} d_t \boldsymbol{v}^{n+1} \cdot \boldsymbol{\phi} + \rho_F \int_{\Omega_F(t^{n+1})} \left((\boldsymbol{v}^n - \boldsymbol{w}^{n+1}) \cdot \nabla \right) \boldsymbol{v}^{n+1} \cdot \boldsymbol{\phi} + a_F^{n+1}(\boldsymbol{v}^{n+1}, \boldsymbol{\phi}) \\
& \quad - b_F^{n+1}(p_F^{n+1}, \boldsymbol{\phi}) + b_F^{n+1}(\psi, \boldsymbol{v}^{n+1}) \\
& = \int_{\Omega_F(t^{n+1})} \boldsymbol{f}^{n+1} \cdot \boldsymbol{\phi} + \int_{\Sigma_F^N(t^{n+1})} \boldsymbol{g}^{n+1} \cdot \boldsymbol{\phi} - \int_{\Gamma(t^{n+1})} L \left(\boldsymbol{v}^{n+1} - \boldsymbol{\xi}^{n+1} - \boldsymbol{q}^{n+1} \right) \cdot \boldsymbol{n}_F^{n+1} \left(\boldsymbol{\phi} \cdot \boldsymbol{n}_F^{n+1} \right) \\
& \quad + \int_{\Gamma(t^{n+1})} (\boldsymbol{n}_F^n \cdot \boldsymbol{\sigma}_F^n \boldsymbol{n}_F^n)(\boldsymbol{\phi} \cdot \boldsymbol{n}_F^{n+1}) - \sum_{i=1}^{d-1} \int_{\Gamma(t^{n+1})} \gamma (\boldsymbol{v}^{n+1} - \boldsymbol{\xi}^{n+1}) \cdot \boldsymbol{\tau}_{F,i}^{n+1} \left(\boldsymbol{\phi} \cdot \boldsymbol{\tau}_{F,i}^{n+1} \right).
\end{aligned}
$$

Set $n = n + 1$ and go back to Step 1.

The proposed method can be further partitioned to split the Biot problem into a structure subproblem and a Darcy subproblem. In that way, the domain can be updated after the new displacement is computed in the mechanics subproblem, and the Darcy subproblem can be solved on the current domain. The fully decoupled method is given in Algorithm 3.2.

Remark 1. We note that in both (3.7) and (3.10), the boundary conditions in Step 1 can be recast onto the reference boundary $\hat{\Gamma}$ to simplify the numerical implementation.

4. Stability analysis. In this section, to simplify the analysis, we will assume that the flow is described using the Stokes equations and that the fluid and the poroelastic domain are fixed. We will also assume that the structure is linearly viscoelastic, with the Cauchy stress tensor given by

$$\boldsymbol{\sigma}_E(\boldsymbol{\eta}, \boldsymbol{\xi}) = 2\mu_P \boldsymbol{D}(\boldsymbol{\eta}) + \lambda_P \nabla \cdot \boldsymbol{\eta} \boldsymbol{I} + 2\mu_V \boldsymbol{D}(\boldsymbol{\xi}), \tag{4.1}$$

where μ_P and λ_P are Lamé's parameters and μ_V is the viscous modulus of the structure. These assumptions are commonly used in the analysis of partitioned methods for fluid-structure interaction and FPSI problems [12, 2]. Even with these assumptions, the problem still remains challenging due to the complexity of the domain decomposition. For simplicity, we will drop the hat notation in this section.

We note that, in this case, Algorithm 3.1 can be written in the strong form as follows.

STEP 1 (Biot subproblem (linear)). Find $\boldsymbol{\xi}^{n+1} = d_t \boldsymbol{\eta}^{n+1}, \boldsymbol{q}^{n+1}$, and p_P^{n+1} such that

$$\rho_P d_t \boldsymbol{\xi}^{n+1} = \nabla \cdot \left(\boldsymbol{\sigma}_E(\boldsymbol{\eta}^{n+1}, \boldsymbol{\xi}^{n+1}) - \alpha p_P^{n+1} \boldsymbol{I} \right) \quad \text{in } \Omega_P, \tag{4.2a}$$

$$\boldsymbol{\kappa}^{-1} \boldsymbol{q}^{n+1} = -\nabla p_P^{n+1} \quad \text{in } \Omega_P, \tag{4.2b}$$

$$c_0 d_t p_P^{n+1} + \alpha \nabla \cdot \boldsymbol{\xi}^{n+1} + \nabla \cdot \boldsymbol{q}^{n+1} = 0 \quad \text{in } \Omega_P, \tag{4.2c}$$

$$\boldsymbol{n}_F \cdot \boldsymbol{\sigma}_P^{n+1} \boldsymbol{n}_F + L \left(\boldsymbol{\xi}^{n+1} + \boldsymbol{q}^{n+1} \right) \cdot \boldsymbol{n}_P = \boldsymbol{n}_F \cdot \boldsymbol{\sigma}_F^n \boldsymbol{n}_F + L \boldsymbol{v}^n \cdot \boldsymbol{n}_P \quad \text{on } \Gamma, \tag{4.2d}$$

$$\boldsymbol{\tau}_{P,i} \cdot \boldsymbol{\sigma}_P^{n+1} \boldsymbol{n}_F = \gamma (\boldsymbol{v}^n - \boldsymbol{\xi}^{n+1}) \cdot \boldsymbol{\tau}_{P,i} \quad \text{for } i = 1, \ldots, d-1 \quad \text{on } \Gamma, \tag{4.2e}$$

$$\delta \boldsymbol{q}^{n+1} \cdot \boldsymbol{n}_P - p_P^{n+1} + L \left(\boldsymbol{\xi}^{n+1} + \boldsymbol{q}^{n+1} \right) \cdot \boldsymbol{n}_P = \boldsymbol{n}_F \cdot \boldsymbol{\sigma}_F^n \boldsymbol{n}_F + L \boldsymbol{v}^n \cdot \boldsymbol{n}_P \quad \text{on } \Gamma. \tag{4.2f}$$

STEP 2 (fluid subproblem (linear)). Find $\boldsymbol{v}^{n+1}$ and p_F^{n+1} such that

$$\rho_F d_t \boldsymbol{v}^{n+1} = \nabla \cdot \boldsymbol{\sigma}_F(\boldsymbol{v}^{n+1}, p_F^{n+1}) + \boldsymbol{f}^{n+1} \quad \text{in } \Omega_F, \tag{4.3a}$$

$$\nabla \cdot \boldsymbol{v}^{n+1} = 0 \quad \text{in } \Omega_F, \tag{4.3b}$$

$$\boldsymbol{n}_F \cdot \boldsymbol{\sigma}_F^{n+1} \boldsymbol{n}_F + L \boldsymbol{v}^{n+1} \cdot \boldsymbol{n}_F = \boldsymbol{n}_F \cdot \boldsymbol{\sigma}_F^n \boldsymbol{n}_F + L \left(\boldsymbol{\xi}^{n+1} + \boldsymbol{q}^{n+1} \right) \cdot \boldsymbol{n}_F \quad \text{on } \Gamma, \tag{4.3c}$$

$$\boldsymbol{\tau}_{F,i} \cdot \boldsymbol{\sigma}_F^{n+1} \boldsymbol{n}_F = -\gamma (\boldsymbol{v}^{n+1} - \boldsymbol{\xi}^{n+1}) \cdot \boldsymbol{\tau}_{F,i}, \quad i = 1, \ldots, d-1 \quad \text{on } \Gamma. \tag{4.3d}$$

Problems (4.2) and (4.3) are solved with boundary conditions (2.3d)–(2.3e) and (2.2c)–(2.2d), respectively. In the case when the Biot problem is split into a structure

subproblem and a Darcy subproblem (described in Algorithm 3.2), Step 1 can be written as follows.

STEP 1A (structure subproblem (linear)). Find $\boldsymbol{\xi}^{n+1} = d_t\boldsymbol{\eta}^{n+1}$ such that

$$\rho_P d_t\boldsymbol{\xi}^{n+1} = \nabla\cdot\left(\boldsymbol{\sigma}_E(\boldsymbol{\eta}^{n+1},\boldsymbol{\xi}^{n+1}) - \alpha p_P^n\boldsymbol{I}\right) \quad \text{in } \Omega_P, \tag{4.4a}$$

$$\boldsymbol{n}_F\cdot\boldsymbol{\sigma}_P^{n+1}\boldsymbol{n}_F + L\left(\boldsymbol{\xi}^{n+1}+\boldsymbol{q}^n\right)\cdot\boldsymbol{n}_P = \boldsymbol{n}_F\cdot\boldsymbol{\sigma}_F^n\boldsymbol{n}_F + L\boldsymbol{v}^n\cdot\boldsymbol{n}_P \quad \text{on } \Gamma, \tag{4.4b}$$

$$\boldsymbol{\tau}_{P,i}\cdot\boldsymbol{\sigma}_P^{n+1}\boldsymbol{n}_F = \gamma(\boldsymbol{v}^n-\boldsymbol{\xi}^{n+1})\cdot\boldsymbol{\tau}_{P,i} \quad \text{for } i=1,\dots,d-1 \quad \text{on } \Gamma. \tag{4.4c}$$

STEP 1B (Darcy subproblem (linear)). Find $\boldsymbol{q}^{n+1}$ and p_P^{n+1} such that

$$\boldsymbol{\kappa}^{-1}\boldsymbol{q}^{n+1} = -\nabla p_P^{n+1} \quad \text{in } \Omega_P, \tag{4.5a}$$

$$c_0 d_t p_P^{n+1} + \alpha\nabla\cdot\boldsymbol{\xi}^{n+1} + \nabla\cdot\boldsymbol{q}^{n+1} = 0 \quad \text{in } \Omega_P, \tag{4.5b}$$

$$\delta\boldsymbol{q}^{n+1}\cdot\boldsymbol{n}_P - p_P^{n+1} + L\left(\boldsymbol{\xi}^{n+1}+\boldsymbol{q}^{n+1}\right)\cdot\boldsymbol{n}_P = \boldsymbol{n}_F\cdot\boldsymbol{\sigma}_F^n\boldsymbol{n}_F + L\boldsymbol{v}^n\cdot\boldsymbol{n}_P \quad \text{on } \Gamma. \tag{4.5c}$$

In this section, we will use the polarization identity

$$2(a-b)a = a^2 - b^2 + (a-b)^2 \tag{4.6}$$

and the following notation for the solid elastic energy:

$$\|\boldsymbol{\eta}^n\|_S^2 = 2\mu_P\|\boldsymbol{D}(\boldsymbol{\eta}^n)\|^2_{L^2(\Omega_P)} + \lambda_P\|\nabla\cdot\boldsymbol{\eta}^n\|^2_{L^2(\Omega_P)}.$$

Let $\mathcal{E}^n$ denote the sum of kinetic and elastic energy of the solid and kinetic energy of the fluid, given by

$$\mathcal{E}^n = \frac{\rho_P}{2}\|\boldsymbol{\xi}^n\|^2_{L^2(\Omega_P)} + \frac{1}{2}\|\boldsymbol{\eta}^n\|_S^2 + \frac{c_0}{2}\|p_P^n\|^2_{L^2(\Omega_P)} + \frac{\rho_F}{2}\|\boldsymbol{v}^n\|^2_{L^2(\Omega_F)};$$

let $\mathcal{D}^n$ denote the fluid dissipation and dissipation due to the fluid entry resistance and the slip between the fluid and solid in the tangential direction at the fluid-structure boundary, given by

$$\begin{aligned}\mathcal{D}^n = {}& \mu_F\Delta t\sum_{k=1}^n\|\boldsymbol{D}(\boldsymbol{v}^k)\|^2_{L^2(\Omega_F)} + \Delta t\sum_{k=1}^n\left\|\boldsymbol{\kappa}^{-\frac{1}{2}}\boldsymbol{q}^k\right\|^2_{L^2(\Omega_P)} + \frac{\Delta t\delta}{2}\sum_{k=1}^{n-1}\|\boldsymbol{q}^k\cdot\boldsymbol{n}_P\|^2_{L^2(\Gamma)}\\ &+ \Delta t\gamma\left(\sum_{i=1}^{d-1}\sum_{k=1}^n\|(\boldsymbol{v}^k-\boldsymbol{\xi}^k)\cdot\boldsymbol{\tau}_{F,i}\|^2_{L^2(\Gamma)} + \sum_{i=1}^{d-1}\sum_{k=1}^n\|(\boldsymbol{\xi}^k-\boldsymbol{v}^{k-1})\cdot\boldsymbol{\tau}_{F,i}\|^2_{L^2(\Gamma)}\right);\end{aligned}$$

let $\mathcal{N}_1^n$ and $\mathcal{N}_2^n$ denote the remaining terms due to numerical dissipation,

$$\mathcal{N}_1^n = \frac{\Delta t\gamma}{2}\sum_{i=1}^{d-1}\|\boldsymbol{v}^n\cdot\boldsymbol{\tau}_{F,i}\|^2_{L^2(\Gamma)} + \frac{\Delta tL}{2}\|\boldsymbol{v}^n\cdot\boldsymbol{n}_F\|^2_{L^2(\Gamma)} + \frac{\Delta t}{2L}\|\boldsymbol{n}_P\cdot\boldsymbol{\sigma}_F^n\boldsymbol{n}_P\|^2_{L^2(\Gamma)},$$

$$\begin{aligned}\mathcal{N}_2^n = {}& \frac{\rho_P}{2}\sum_{k=1}^n\|\boldsymbol{\xi}^k-\boldsymbol{\xi}^{k-1}\|^2_{L^2(\Omega_P)} + \frac{1}{2}\sum_{k=1}^n\|\boldsymbol{\eta}^k-\boldsymbol{\eta}^{k-1}\|_S^2 + \frac{c_0}{4}\sum_{k=1}^n\|p_P^k-p_P^{k-1}\|^2_{L^2(\Omega_P)}\\ &+ \frac{\rho_F}{2}\sum_{k=1}^n\|\boldsymbol{v}^k-\boldsymbol{v}^{k-1}\|^2_{L^2(\Omega_F)} + \frac{\Delta tL}{2}\sum_{k=1}^n\|\left(\boldsymbol{\xi}^k+\boldsymbol{q}^k-\boldsymbol{v}^{k-1}\right)\cdot\boldsymbol{n}_P\|^2_{L^2(\Gamma)};\end{aligned}$$

and let $\mathcal{F}^n$ denote the forcing terms

$$\mathcal{F}^n = \frac{\Delta t C_K^2}{2\mu_F} \sum_{k=1}^{n} \|\boldsymbol{f}^k\|^2_{L^2(\Omega_F)} + \frac{\Delta t C_{tr}^2 C_P C_K^2}{2\mu_F} \sum_{k=1}^{n} \|\boldsymbol{g}^k\|^2_{L^2(\Sigma_F^N)},$$

where C_P, C_K, and C_{tr} are Poincaré–Friedrichs (A.3), Korn's (A.5), and trace (A.4) inequality constants, respectively.

THEOREM 4.1. *Let $(\boldsymbol{\xi}^n, \boldsymbol{\eta}^n, \boldsymbol{v}^n, p^n)$ be the solution of the fully partitioned method described by* (4.4)*,* (4.5)*, and* (4.3)*. Assume that the following conditions are satisfied:*

$$C_V := \mu_V - \frac{2L^2 C_{tr}^2 C_P C_K^2}{\delta} > 0, \quad \Delta t < \frac{C_V c_0}{\alpha^2 d C_K^2}. \tag{4.7}$$

Then, the following a priori energy estimate holds:

$$\begin{aligned}
&\mathcal{E}^N + \mathcal{D}^N + \mathcal{N}_1^N + \mathcal{N}_2^N + \Delta t \left(C_V - \frac{\Delta t \alpha^2 d C_K^2}{c_0} \right) \sum_{n=0}^{N-1} \|\boldsymbol{D}(\boldsymbol{\xi}^{n+1})\|^2_{L^2(\Omega_P)} \\
&\qquad + \frac{3\Delta t \delta}{4} \|\boldsymbol{q}^N \cdot \boldsymbol{n}_P\|^2_{L^2(\Gamma)} \\
&\quad \le \mathcal{E}^0 + \mathcal{N}_1^0 + \mathcal{F}^N + \frac{\Delta t \delta}{4} \|\boldsymbol{q}^0 \cdot \boldsymbol{n}_P\|^2_{L^2(\Gamma)}.
\end{aligned}$$

Proof. We multiply (4.4a) by $\Delta t \boldsymbol{\xi}^{n+1}$, (4.5a) by $\Delta t \boldsymbol{q}^{n+1}$, and (4.5b) by $\Delta t p_P^{n+1}$ and integrate over Ω_P. Similarly, we multiply (4.3a) by $\Delta t \boldsymbol{v}^{n+1}$ and (4.3b) by $\Delta t p_F^{n+1}$ and integrate over Ω_F. Adding the equations together, integrating by parts, and incorporating the interface conditions (4.4b)–(4.4c), (4.5c), and (4.3c)–(4.3d) as well as the boundary conditions, we have

(4.8)

$$\begin{aligned}
&\frac{\rho_P}{2} \left(\|\boldsymbol{\xi}^{n+1}\|^2_{L^2(\Omega_P)} - \|\boldsymbol{\xi}^n\|^2_{L^2(\Omega_P)} + \|\boldsymbol{\xi}^{n+1} - \boldsymbol{\xi}^n\|^2_{L^2(\Omega_P)} \right) + \frac{1}{2} \left(\|\boldsymbol{\eta}^{n+1}\|^2_S - \|\boldsymbol{\eta}^n\|^2_S + \|\boldsymbol{\eta}^{n+1} - \boldsymbol{\eta}^n\|^2_S \right) \\
&\quad + \frac{c_0}{2} \left(\|p_P^{n+1}\|^2_{L^2(\Omega_P)} - \|p_P^n\|^2_{L^2(\Omega_P)} + \|p_P^{n+1} - p_P^n\|^2_{L^2(\Omega_P)} \right) + \mu_V \Delta t \|\boldsymbol{D}(\boldsymbol{\xi}^{n+1})\|^2_{L^2(\Omega_P)} \\
&\quad + \Delta t \|\boldsymbol{\kappa}^{-\frac{1}{2}} \boldsymbol{q}^{n+1}\|^2_{L^2(\Omega_P)} + \frac{\rho_F}{2} \left(\|\boldsymbol{v}^{n+1}\|^2_{L^2(\Omega_F)} - \|\boldsymbol{v}^n\|^2_{L^2(\Omega_F)} + \|\boldsymbol{v}^{n+1} - \boldsymbol{v}^n\|^2_{L^2(\Omega_F)} \right) \\
&\quad + 2\mu_F \Delta t \|\boldsymbol{D}(\boldsymbol{v}^{n+1})\|^2_{L^2(\Omega_F)} + \Delta t \delta \|\boldsymbol{q}^{n+1} \cdot \boldsymbol{n}_P\|^2_{L^2(\Gamma)} \\
&= -\Delta t \int_{\Omega_P} \alpha \nabla \cdot \boldsymbol{\xi}^{n+1} \left(p_P^{n+1} - p_P^n \right) + \Delta t \int_\Gamma \boldsymbol{n}_P \cdot \boldsymbol{\sigma}_F^n \boldsymbol{n}_P \left(\boldsymbol{\xi}^{n+1} + \boldsymbol{q}^{n+1} - \boldsymbol{v}^{n+1} \right) \cdot \boldsymbol{n}_P \\
&\quad - \Delta t \int_\Gamma L \left(\boldsymbol{\xi}^{n+1} + \boldsymbol{q}^n - \boldsymbol{v}^n \right) \cdot \boldsymbol{n}_P \boldsymbol{\xi}^{n+1} \cdot \boldsymbol{n}_P - \Delta t \int_\Gamma L \left(\boldsymbol{\xi}^{n+1} + \boldsymbol{q}^{n+1} - \boldsymbol{v}^n \right) \cdot \boldsymbol{n}_P \boldsymbol{q}^{n+1} \cdot \boldsymbol{n}_P \\
&\quad - \Delta t \int_\Gamma L \left(\boldsymbol{v}^{n+1} - \boldsymbol{\xi}^{n+1} - \boldsymbol{q}^{n+1} \right) \cdot \boldsymbol{n}_F \boldsymbol{v}^{n+1} \cdot \boldsymbol{n}_F \\
&\quad + \Delta t \sum_{i=1}^{d-1} \int_\Gamma \gamma (\boldsymbol{v}^n - \boldsymbol{\xi}^{n+1}) \cdot \boldsymbol{\tau}_{P,i} \boldsymbol{\xi}^{n+1} \cdot \boldsymbol{\tau}_{P,i} - \Delta t \sum_{i=1}^{d-1} \int_\Gamma \gamma (\boldsymbol{v}^{n+1} - \boldsymbol{\xi}^{n+1}) \cdot \boldsymbol{\tau}_{F,i} \boldsymbol{v}^{n+1} \cdot \boldsymbol{\tau}_{F,i} \\
&\quad + \Delta t \int_{\Omega_F} \boldsymbol{f}^{n+1} \cdot \boldsymbol{v}^{n+1} + \Delta t \int_{\Sigma_F^N} \boldsymbol{g}^{n+1} \cdot \boldsymbol{v}^{n+1}.
\end{aligned}$$

We bound the right-hand side as follows. To estimate the first term, we use the Cauchy–Schwarz (A.2) and Young's (A.1) inequalities. Together with $\|\nabla \cdot \boldsymbol{\xi}^{n+1}\| \le \sqrt{d} \|\nabla \boldsymbol{\xi}^{n+1}\|$ and Korn's inequality (A.5), we have

(4.9)
$$-\Delta t\int_{\Omega_P}\alpha\nabla\cdot\boldsymbol{\xi}^{n+1}\left(p_P^{n+1}-p_P^n\right)\leq\frac{\Delta t^2\alpha^2 dC_K^2}{c_0}\|\boldsymbol{D}(\boldsymbol{\xi}^{n+1})\|^2_{L^2(\Omega_P)}+\frac{c_0}{4}\|p_P^{n+1}-p_P^n\|^2_{L^2(\Omega_P)}.$$

Using the polarization identity (4.6), we estimate the tangential components as follows:

(4.10)
$$\begin{aligned}
&-\Delta t\sum_{i=1}^{d-1}\int_\Gamma\gamma(\boldsymbol{v}^{n+1}-\boldsymbol{\xi}^{n+1})\cdot\boldsymbol{\tau}_{F,i}\boldsymbol{v}^{n+1}\cdot\boldsymbol{\tau}_{F,i}+\Delta t\sum_{i=1}^{d-1}\int_\Gamma\gamma(\boldsymbol{v}^{n}-\boldsymbol{\xi}^{n+1})\cdot\boldsymbol{\tau}_{P,i}\boldsymbol{\xi}^{n+1}\cdot\boldsymbol{\tau}_{P,i}\\
&\quad=-\frac{\Delta t\gamma}{2}\sum_{i=1}^{d-1}\left(\|\boldsymbol{v}^{n+1}\cdot\boldsymbol{\tau}_{F,i}\|^2_{L^2(\Gamma)}-\|\boldsymbol{\xi}^{n+1}\cdot\boldsymbol{\tau}_{F,i}\|^2_{L^2(\Gamma)}+\|(\boldsymbol{v}^{n+1}-\boldsymbol{\xi}^{n+1})\cdot\boldsymbol{\tau}_{F,i}\|^2_{L^2(\Gamma)}\right)\\
&\qquad-\frac{\Delta t\gamma}{2}\sum_{i=1}^{d-1}\left(\|\boldsymbol{\xi}^{n+1}\cdot\boldsymbol{\tau}_{F,i}\|^2_{L^2(\Gamma)}-\|\boldsymbol{v}^{n}\cdot\boldsymbol{\tau}_{F,i}\|^2_{L^2(\Gamma)}+\|(\boldsymbol{\xi}^{n+1}-\boldsymbol{v}^{n})\cdot\boldsymbol{\tau}_{F,i}\|^2_{L^2(\Gamma)}\right)\\
&\quad=-\frac{\Delta t\gamma}{2}\sum_{i=1}^{d-1}\Big(\|\boldsymbol{v}^{n+1}\cdot\boldsymbol{\tau}_{F,i}\|^2_{L^2(\Gamma)}-\|\boldsymbol{v}^{n}\cdot\boldsymbol{\tau}_{F,i}\|^2_{L^2(\Gamma)}+\|(\boldsymbol{v}^{n+1}-\boldsymbol{\xi}^{n+1})\cdot\boldsymbol{\tau}_{F,i}\|^2_{L^2(\Gamma)}\\
&\qquad\qquad+\|(\boldsymbol{\xi}^{n+1}-\boldsymbol{v}^{n})\cdot\boldsymbol{\tau}_{F,i}\|^2_{L^2(\Gamma)}\Big).
\end{aligned}$$

Using (4.3c) and (4.6), the term involving the fluid normal stress gives us

$$\begin{aligned}
&\Delta t\int_\Gamma\boldsymbol{n}_P\cdot\boldsymbol{\sigma}_F^n\boldsymbol{n}_P\left(\boldsymbol{\xi}^{n+1}-\boldsymbol{v}^{n+1}+\boldsymbol{q}^{n+1}\right)\cdot\boldsymbol{n}_P\\
&\quad=\frac{\Delta t}{L}\int_\Gamma\boldsymbol{n}_P\cdot\boldsymbol{\sigma}_F^n\boldsymbol{n}_P\left(\boldsymbol{n}_F\cdot\boldsymbol{\sigma}_F^n\boldsymbol{n}_F-\boldsymbol{n}_F\cdot\boldsymbol{\sigma}_F^{n+1}\boldsymbol{n}_F\right)\\
&\quad=\frac{\Delta t}{2L}\left(\|\boldsymbol{n}_P\cdot\boldsymbol{\sigma}_F^n\boldsymbol{n}_P\|^2_{L^2(\Gamma)}-\|\boldsymbol{n}_P\cdot\boldsymbol{\sigma}_F^{n+1}\boldsymbol{n}_P\|^2_{L^2(\Gamma)}+\|\boldsymbol{n}_F\cdot\boldsymbol{\sigma}_F^{n+1}\boldsymbol{n}_F-\boldsymbol{n}_F\dot{\boldsymbol{\sigma}}_F^n\boldsymbol{n}_F\|^2_{L^2(\Gamma)}\right)\\
&\quad=\frac{\Delta t}{2L}\left(\|\boldsymbol{n}_P\cdot\boldsymbol{\sigma}_F^n\boldsymbol{n}_P\|^2_{L^2(\Gamma)}-\|\boldsymbol{n}_P\cdot\boldsymbol{\sigma}_F^{n+1}\boldsymbol{n}_P\|^2_{L^2(\Gamma)}\right)+\frac{\Delta tL}{2}\|(\boldsymbol{\xi}^{n+1}+\boldsymbol{q}^{n+1}-\boldsymbol{v}^{n+1})\cdot\boldsymbol{n}_P\|^2_{L^2(\Gamma)}.
\end{aligned}$$

To bound the terms containing the combination parameter, L, we rearrange and use (4.6) as follows:

(4.11)
$$\begin{aligned}
&-\Delta t\int_\Gamma L\left(\boldsymbol{\xi}^{n+1}+\boldsymbol{q}^{n+1}-\boldsymbol{v}^{n}\right)\cdot\boldsymbol{n}_P(\boldsymbol{\xi}^{n+1}+\boldsymbol{q}^{n+1})\cdot\boldsymbol{n}_P+\Delta t\int_\Gamma L\left(\boldsymbol{q}^{n+1}-\boldsymbol{q}^{n}\right)\cdot\boldsymbol{n}_P\boldsymbol{\xi}^{n+1}\cdot\boldsymbol{n}_P\\
&\quad-\Delta t\int_\Gamma L\left(\boldsymbol{v}^{n+1}-\boldsymbol{\xi}^{n+1}-\boldsymbol{q}^{n+1}\right)\cdot\boldsymbol{n}_F\boldsymbol{v}^{n+1}\cdot\boldsymbol{n}_F\\
&=-\frac{\Delta tL}{2}\left(\|\left(\boldsymbol{\xi}^{n+1}+\boldsymbol{q}^{n+1}\right)\cdot\boldsymbol{n}_P\|^2_{L^2(\Gamma)}-\|\boldsymbol{v}^{n}\cdot\boldsymbol{n}_P\|^2_{L^2(\Gamma)}+\|\left(\boldsymbol{\xi}^{n+1}+\boldsymbol{q}^{n+1}-\boldsymbol{v}^{n}\right)\cdot\boldsymbol{n}_P\|^2_{L^2(\Gamma)}\right)\\
&\quad-\frac{\Delta tL}{2}\left(\|\boldsymbol{v}^{n+1}\cdot\boldsymbol{n}_F\|^2_{L^2(\Gamma)}-\|\left(\boldsymbol{\xi}^{n+1}+\boldsymbol{q}^{n+1}\right)\cdot\boldsymbol{n}_F\|^2_{L^2(\Gamma)}\right.\\
&\qquad\left.+\|\left(\boldsymbol{\xi}^{n+1}+\boldsymbol{q}^{n+1}-\boldsymbol{v}^{n+1}\right)\cdot\boldsymbol{n}_F\|^2_{L^2(\Gamma)}\right)\\
&\quad+\Delta t\int_\Gamma L\left(\boldsymbol{q}^{n+1}-\boldsymbol{q}^{n}\right)\cdot\boldsymbol{n}_P\boldsymbol{\xi}^{n+1}\cdot\boldsymbol{n}_P\\
&=-\frac{\Delta tL}{2}\left(\|\boldsymbol{v}^{n+1}\cdot\boldsymbol{n}_F\|^2_{L^2(\Gamma)}-\|\boldsymbol{v}^{n}\cdot\boldsymbol{n}_F\|^2_{L^2(\Gamma)}+\|\left(\boldsymbol{\xi}^{n+1}+\boldsymbol{q}^{n+1}-\boldsymbol{v}^{n}\right)\cdot\boldsymbol{n}_P\|^2_{L^2(\Gamma)}\right)\\
&\quad-\frac{\Delta tL}{2}\|\left(\boldsymbol{\xi}^{n+1}+\boldsymbol{q}^{n+1}-\boldsymbol{v}^{n+1}\right)\cdot\boldsymbol{n}_P\|^2_{L^2(\Gamma)}+\Delta t\int_\Gamma L\left(\boldsymbol{q}^{n+1}-\boldsymbol{q}^{n}\right)\cdot\boldsymbol{n}_P\boldsymbol{\xi}^{n+1}\cdot\boldsymbol{n}_P.
\end{aligned}$$

To bound the last term in (4.11), we use the Cauchy–Schwarz (A.2), Young's (A.1), trace (A.4), Poincaré–Friedrichs (A.3), and Korn's (A.5) inequalities as follows:

$$\Delta t \int_\Gamma L\left(\boldsymbol{q}^{n+1}-\boldsymbol{q}^n\right)\cdot\boldsymbol{n}_P\boldsymbol{\xi}^{n+1}\cdot\boldsymbol{n}_P \le \frac{\Delta t\delta}{8}\|(\boldsymbol{q}^{n+1}-\boldsymbol{q}^n)\cdot\boldsymbol{n}_P\|^2_{L^2(\Gamma)} + \frac{2\Delta t L^2 C_{tr}^2 C_P C_K^2}{\delta}\|\boldsymbol{D}(\boldsymbol{\xi}^{n+1})\|^2_{L^2(\Omega_P)}. \tag{4.12}$$

Finally, we bound the forcing terms using the Cauchy–Schwarz (A.2), Young's (A.1), trace (A.4), Poincaré–Friedrichs (A.3), and Korn's (A.5) inequalities as follows:

$$\begin{aligned}&\Delta t\int_{\Omega_F}\boldsymbol{f}^{n+1}\cdot\boldsymbol{v}^{n+1}+\Delta t\int_{\Sigma_F^N}\boldsymbol{g}^{n+1}\cdot\boldsymbol{v}^{n+1}\\ &\quad\le\frac{\Delta t C_K^2}{2\mu_F}\|\boldsymbol{f}^{n+1}\|^2_{L^2(\Omega_F)}+\frac{\Delta t C_{tr}^2 C_P C_K^2}{2\mu_F}\|\boldsymbol{g}^{n+1}\|^2_{L^2(\Sigma_F^N)}+\mu_F\Delta t\|\boldsymbol{D}(\boldsymbol{v}^{n+1})\|^2_{L^2(\Omega_F)}.\end{aligned} \tag{4.13}$$

Combining (4.9)–(4.13) with (4.8) and summing from $n=0,\dots N-1$, we get

$$\begin{aligned}&\mathcal{E}^N+\mathcal{D}^N+\mathcal{N}_1^N+\mathcal{N}_2^N+\frac{\Delta t\delta}{2}\sum_{n=0}^{N-2}\|\boldsymbol{q}^{n+1}\cdot\boldsymbol{n}_P\|^2_{L^2(\Gamma)}+\Delta t\delta\|\boldsymbol{q}^N\cdot\boldsymbol{n}_P\|^2_{L^2(\Gamma)}\\ &\qquad+\left(\mu_V-\frac{\Delta t\alpha^2 d C_K^2}{c_0}-\frac{2L^2C_{tr}^2C_PC_K^2}{\delta}\right)\Delta t\sum_{n=0}^{N-1}\|\boldsymbol{D}(\boldsymbol{\xi}^{n+1})\|^2_{L^2(\Omega_P)}\end{aligned} \tag{4.14}$$

$$\le\mathcal{E}^0+\mathcal{N}_1^0+\mathcal{F}^N+\frac{\Delta t\delta}{8}\sum_{n=0}^{N-1}\|(\boldsymbol{q}^{n+1}-\boldsymbol{q}^n)\cdot\boldsymbol{n}_P\|^2_{L^2(\Gamma)}. \tag{4.15}$$

For the last term on the right-hand side, we proceed as follows. Using the inequality $(a+b)^2\le 2(a^2+b^2)$ and rearranging the terms in the summation, we have

$$\begin{aligned}\frac{\Delta t\delta}{8}\sum_{n=0}^{N-1}\|(\boldsymbol{q}^{n+1}-\boldsymbol{q}^n)\cdot\boldsymbol{n}_P\|^2_{L^2(\Gamma)}&\le\frac{\Delta t\delta}{4}\sum_{n=0}^{N-1}\left(\|\boldsymbol{q}^{n+1}\cdot\boldsymbol{n}_P\|^2_{L^2(\Gamma)}+\|\boldsymbol{q}^n\cdot\boldsymbol{n}_P\|^2_{L^2(\Gamma)}\right)\\ &\le\frac{\Delta t\delta}{2}\sum_{n=0}^{N-2}\|\boldsymbol{q}^{n+1}\cdot\boldsymbol{n}_P\|^2_{L^2(\Gamma)}+\frac{\Delta t\delta}{4}\|\boldsymbol{q}^0\cdot\boldsymbol{n}_P\|^2_{L^2(\Gamma)}\\ &\quad+\frac{\Delta t\delta}{4}\|\boldsymbol{q}^N\cdot\boldsymbol{n}_P\|^2_{L^2(\Gamma)}.\end{aligned} \tag{4.16}$$

Using (4.5a) and combining (4.16) with (4.15) yields the desired energy estimate. ∎

Remark 2. For the first condition in (4.7) to hold, the combination parameter, L, needs to satisfy

$$L<\sqrt{\frac{\mu_V\delta}{2C_{tr}^2C_PC_K^2}}. \tag{4.17}$$

The second condition in (4.7) is independent of the mesh size, but it yields restrictive values of the time step for small values of c_0 and C_V. However, we note that no stability issues were observed when Algorithm 3.2 was used with $\mu_V=0$ and $c_0=10^{-3}$ in section 5. Even though our simulation results are limited, they indicate that the parameter dependence in (4.7) is likely not sharp.

Remark 3. To extend the analysis to the nonlinear, moving domain problem, condition (2.6) would need to be changed to

$$\boldsymbol{n}_F \cdot \boldsymbol{\sigma}_F \boldsymbol{n}_F + \frac{\rho_F}{2}|\boldsymbol{v}|^2 + p_P = \delta \boldsymbol{q} \cdot \boldsymbol{n}_P \quad \text{on } \Gamma(t) \times (0,T)$$

in order to obtain energy estimates even at the continuous level. Additional difficulties would come from estimation of terms associated with the linearization of nonlinearities due to the domain motion, as well as the terms due to splitting of the solid and Darcy problems in the Biot's system, i.e.,

$$-\int_{\hat{\Omega}_P} \alpha \hat{J}^n \hat{p}_P^n (\hat{\boldsymbol{F}}^n)^{-T} : \hat{\nabla} \hat{\boldsymbol{\xi}}^{n+1} d\hat{\boldsymbol{x}} + \int_{\hat{\Omega}_P} \alpha \hat{J}^{n+1} \hat{p}_P^{n+1} (\hat{\boldsymbol{F}}^{n+1})^{-T} : \hat{\nabla} \hat{\boldsymbol{\xi}}^{n+1} d\hat{\boldsymbol{x}}.$$

If the Biot–Stokes partitioned method (4.2)–(4.3) is considered instead of the fully partitioned scheme analyzed in Theorem 4.1, the terms estimated in (4.9) and (4.12) would be equal to zero. Hence, the unconditional stability is achieved independently of the structure viscous modulus, μ_V, and the storativity coefficient, c_0. In that case, purely elastic structures could be considered. The stability of method (4.2)–(4.3) is given in the following corollary.

COROLLARY 4.2. *Let* $(\boldsymbol{\xi}^n, \boldsymbol{\eta}^n, \boldsymbol{v}^n, p^n)$ *be the solution of the Biot–Stokes partitioned method described by* (4.2)–(4.3). *Then, the method* (4.2)–(4.3) *is unconditionally stable and the following a priori energy estimate holds:*

$$\begin{aligned}\mathcal{E}^N + \mathcal{D}^N + \mathcal{N}_1^N + \mathcal{N}_2^N + \frac{c_0}{4}\sum_{k=1}^{n} \|p_P^k - p_P^{k-1}\|^2_{L^2(\Omega_P)} + \frac{\Delta t \delta}{2}\sum_{n=0}^{N-2} \|\boldsymbol{q}^{n+1} \cdot \boldsymbol{n}_P\|^2_{L^2(\Gamma)} \\ + \Delta t \delta \|\boldsymbol{q}^N \cdot \boldsymbol{n}_P\|^2_{L^2(\Gamma)} \\ + \Delta t \mu_V \sum_{n=0}^{N-1} \|\boldsymbol{D}(\boldsymbol{\xi}^{n+1})\|^2_{L^2(\Omega_P)} \leq \mathcal{E}^0 + \mathcal{N}_1^0 + \mathcal{F}^N.\end{aligned}$$

We note that the results in Corollary 4.2 can be easily extended to nonlinear, hyperelastic structures.

5. Numerical examples. In the numerical examples, we investigate the stability and accuracy properties of the proposed methods. For spatial discretization, we use the finite element method. The finite element solver *FreeFem++* [17] is used for computations. In the first example, using the method of manufactured solutions, we investigate the convergence rates of the proposed methods with respect to the combination parameter, L. We also suggest how to choose L based on three different methods where L is dynamically updated. In the second example, we compare the computational results to the ones obtained using a monolithic scheme. We also investigate the effects of fixed versus moving domain assumptions, as well as linear versus nonlinear solid models.

5.1. Example 1. In the first example, we use the method of manufactured solutions to investigate the accuracy of the proposed methods. We assume that the domain is fixed and that the structure is described using a linearly elastic model (4.1), where $\mu_V = 0$. The structure domain is defined as $\Omega_P = (0,1) \times (-1,0)$ and the fluid domain as $\Omega_F = (0,1) \times (0,1)$ with the interface $\Gamma = (0,1) \times \{0\}$. The true solution is defined as

$$\boldsymbol{\eta}_{ref} = \begin{bmatrix} \sin(\pi t)(\cos(y) - 3x) \\ \sin(\pi t)(y+1) \end{bmatrix}, \quad p_{P,ref} = \sin\left(\pi t + \frac{\pi}{4}\right)\sin(\pi x)\cos(0.5\pi y),$$

$$\boldsymbol{v}_{ref} = \begin{bmatrix} \pi\cos(\pi t)(\cos(y) - 3x) \\ \pi\cos(\pi t)(y+1) \end{bmatrix}, \quad p_{F,ref} = \sin\left(\pi t + \frac{\pi}{4}\right)\sin(\pi x)\cos(0.5\pi y) + 2\pi\cos(\pi t).$$

In this example, the parameters ρ_F, μ_F, ρ_P, μ_P, λ_P, α, c_0, and γ are all set to one, $\boldsymbol{\kappa}$ is equal to an identity matrix, and $\delta = 0$. For spatial discretization, we use MINI elements [3] ($\mathcal{P}_1^b$ - $\mathcal{P}_1$) for the fluid velocity and pressure, $\mathcal{P}_1$ elements for the solid, and the Raviart–Thomas $\mathcal{RT}_0 - \mathcal{P}_0$ elements [26] for the Darcy problem. The final time is $T = 0.2$.

We first compute the convergence rates for both Biot–Stokes partitioned algorithm (4.2)–(4.3) and the structure Darcy–Stokes partitioned algorithm given by (4.4)–(4.5) and (4.3) obtained with different values of the combination parameter, L. In particular, we compute the relative errors for $\boldsymbol{\eta}$, $\boldsymbol{\xi}$, and $\boldsymbol{v}$ defined as

$$e_{\boldsymbol{\eta}} = \frac{\|\boldsymbol{\eta} - \boldsymbol{\eta}_{ref}\|_S^2}{\|\boldsymbol{\eta}_{ref}\|_S^2}, \quad e_{\boldsymbol{\xi}} = \frac{\|\boldsymbol{\xi} - \boldsymbol{\xi}_{ref}\|_{L^2(\Omega_P)}^2}{\|\boldsymbol{\xi}_{ref}\|_{L^2(\Omega_P)}^2}, \quad e_F = \frac{\|\boldsymbol{v} - \boldsymbol{v}_{ref}\|_{L^2(\Omega_F)}^2}{\|\boldsymbol{v}_{ref}\|_{L^2(\Omega_F)}^2}.$$

We note that the Biot–Stokes partitioned algorithm (4.2)–(4.3) corresponds to Algorithm 3.1 and that the structure Darcy–Stokes partitioned algorithm given by (4.4)–(4.5) and (4.3) corresponds to Algorithm 3.2, obtained with the assumption that the domain is fixed. To compute the rates of convergence, we use the following time and space discretization parameters:

$$\{\Delta t, \Delta x\} = \left\{\frac{0.01}{2^i}, \frac{0.1}{2^i}\right\}_{i=0}^{3},$$

where Δx is the mesh size.

Figure 2 shows the errors for the displacement (left), structure velocity (middle), and fluid velocity (right) obtained using $L = 0.01, 0.1, 1, 10, 100, 200$, and 500. The top panel shows the results obtained using the Biot–Stokes partitioned algorithm and the bottom panel shows the results obtained using the structure Darcy–Stokes partitioned algorithm. In both cases, very similar behavior is observed, with small differences in the errors for the structure velocity. For both $\boldsymbol{\eta}$ and $\boldsymbol{\xi}$, we observe that $L = 0.01$ gives the worst error and rate but is resolved for all other tested L-values. For $\boldsymbol{\eta}$, the errors and rates are nearly indistinguishable for larger values of L, and almost identical results are obtained for both partitioned methods. The rates for $\boldsymbol{\eta}$ all hug a value of 1, with the exception of $L = 0.01$, which starts off at a rate of 1 but begins to decrease as the time step decreases. Other than $L = 0.01$, when the Biot–Stokes partitioned algorithm is considered, the solid velocity, $\boldsymbol{\xi}$, offers slightly more variance in the results when L=0.1, in which case the smallest error is obtained. The errors are similar for the other values of L, with a slight loss in accuracy which is initially observed for larger values of L, but is resolved as the time step decreases. In the structure Darcy–Stokes partitioned algorithm, the smallest errors for the solid velocity are obtained using $L = 500$, and they grow as L decreases. Other than $L = 0.01$, a small loss in accuracy is observed for $L = 100$ and $L = 200$ and initially for all values of L other than 1. Finally, the errors for the fluid velocity obtained using the two methods look nearly identical. Initially, the rates start off around 1.5 and end around 1 as the mesh size and time step are decreased. Very similar results are obtained for all values of L.

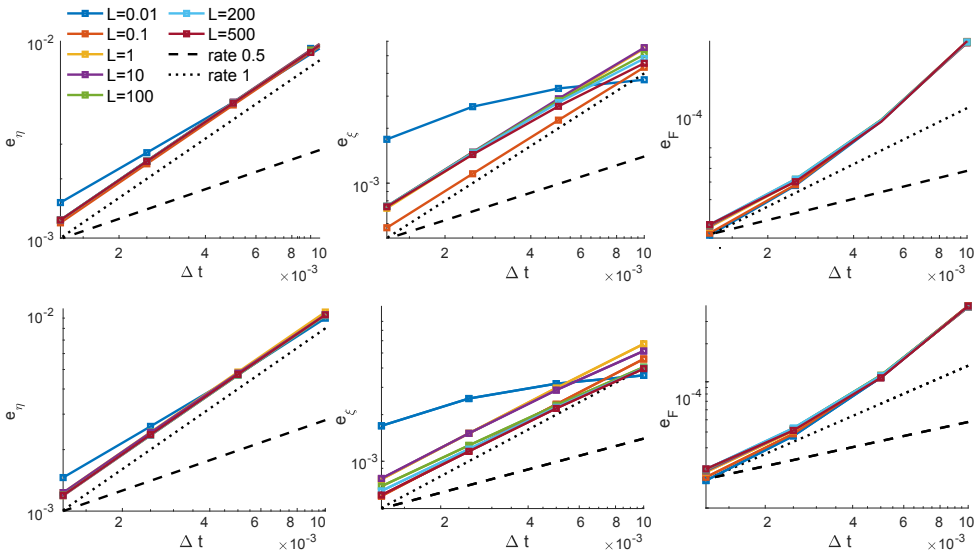

FIG. 2. *Example* 1*: Relative errors for the solid displacement* $\boldsymbol{\eta}$ *(left), solid velocity* $\boldsymbol{\xi}$ *(middle), and fluid velocity* $\boldsymbol{v}$ *(right) at the final time* $T = 0.2$ *s. The top panel shows the results obtained with the Biot–Stokes partitioned scheme, and the bottom panel shows the results obtained with the structure Darcy–Stokes partitioned algorithm.*

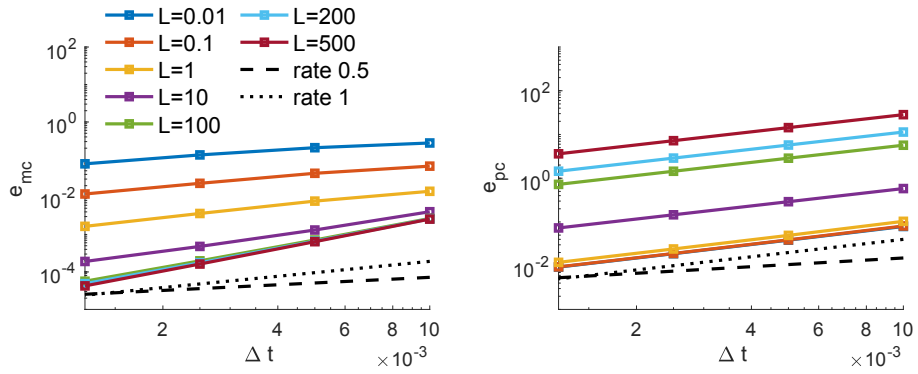

FIG. 3. *Example* 1*: Absolute errors for the mass conservation (left) and the momentum conservation (right) obtained using the structure Darcy–Stokes partitioned algorithm at the final time* $T = 0.2$ *s.*

The Robin boundary conditions used in the derivation of the proposed methods rely on the combination parameter, L, which was used to combine the kinematic condition describing the fluid mass conservation (2.5) and the dynamic condition describing the momentum conservation (2.6) in the fluid phase. Therefore, we also investigate the relation between L and the absolute errors for conditions (2.5) and (2.6), given as

$$e_{mc} = \|(\boldsymbol{\xi} + \boldsymbol{q} - \boldsymbol{v}) \cdot \boldsymbol{n}_F\|_{L^2(\Gamma)}, \quad e_{pc} = \|\boldsymbol{n}_F \cdot \boldsymbol{\sigma}_F \boldsymbol{n}_F + p_P\|_{L^2(\Gamma)},$$

where e_{mc} denotes the error for the mass conservation and e_{pc} the error for the momentum conservation. We note that $L = 0$ in (3.3) recovers the momentum conservation condition, while $L = \infty$ recovers the mass conservation condition. Figure 3 shows the absolute errors for e_{mc} and e_{pc} across different values of L obtained using the

structure Darcy–Stokes partitioned algorithm. The errors obtained using the Biot–Stokes algorithm are nearly identical and hence not shown in the figure. As expected, we observe that the errors for e_{mc} steadily decrease as L increases, and the errors for e_{pc} decrease as L decreases. Furthermore, the rates of convergence for the mass conservation condition increase for larger values of L.

5.2. Determining the values of the combination parameter L. To provide a guideline on how to determine which values of L to use, we consider the relative errors in the approximation of the coupling conditions (2.5) and (2.6), given by

$$e_{mc}^{rel} = \frac{\|(\boldsymbol{\xi} + \boldsymbol{q} - \boldsymbol{v}) \cdot \boldsymbol{n}_F\|_{L^2(\Gamma)}}{\|\boldsymbol{v} \cdot \boldsymbol{n}_F\|_{L^2(\Gamma)}}, \quad e_{pc}^{rel} = \frac{\|\boldsymbol{n}_F \cdot \boldsymbol{\sigma}_F \boldsymbol{n}_F + p_P\|_{L^2(\Gamma)}}{\|\boldsymbol{n}_F \cdot \boldsymbol{\sigma}_F \boldsymbol{n}_F\|_{L^2(\Gamma)}}.$$

We propose to determine L dynamically so that both coupling conditions (2.5) and (2.6) are approximated with comparable accuracy. In particular, we consider the following three formulae to update L at every time step:

$$L_1^{new} = \begin{cases} 2L_1^{old} & \text{if } e_{mc}^{rel} > e_{pc}^{rel}, \\ L_1^{old} & \text{if } e_{mc}^{rel} = e_{pc}^{rel}, \\ \frac{1}{2}L_1^{old} & \text{if } e_{mc}^{rel} < e_{pc}^{rel}, \end{cases} \tag{5.1}$$

$$L_2^{new} = L_2^{old} \left(\frac{e_{mc}^{rel}}{e_{pc}^{rel}} \right)^{\frac{1}{2}}, \tag{5.2}$$

$$L_3^{new} = L_3^{old} \left(\frac{e_{mc}^{rel}}{e_{pc}^{rel}} \right)^{\frac{1}{3}}. \tag{5.3}$$

To test the three different approaches, we consider the same benchmark problem as in section 5.1. We use the time step of $\Delta t = 5 \cdot 10^{-3}$ and the mesh size of $\Delta x = 5 \cdot 10^{-2}$. Initially, we take $L = 1$ in all three cases. Figure 4 shows the evolution of L during the simulation obtained using formulae (5.1), (5.2), and (5.3). The results are obtained using the structure Darcy–Stokes partitioned algorithm and are almost identical to the results using the Biot–Stokes algorithm.

At the final time, we compared the errors for the fluid velocity, e_F, the structure velocity, $e_{\boldsymbol{\xi}}$, and the structure displacement, $e_{\boldsymbol{\eta}}$, obtained using $L = 0.1, 1, 10$ and when L is dynamically updated. The comparison for both partitioned methods is shown in Table 1. We observe that when L is dynamically updated according to (5.1),

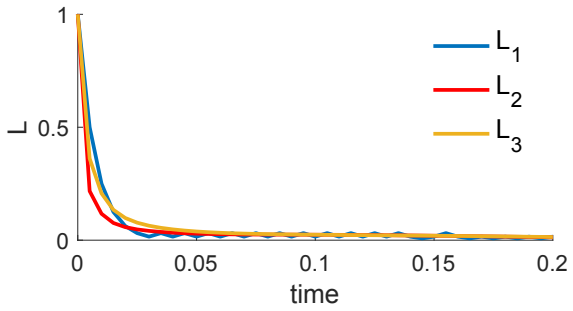

FIG. 4. *Example 1: The evolution of the combination parameter, L, obtained using* (5.1) *(blue line),* (5.2) *(red line), and* (5.3) *(orange line).*

TABLE 1

Example 1: Errors for $\boldsymbol{v}$, $\boldsymbol{\xi}$, and $\boldsymbol{\eta}$ obtained using $L = 0.1, 1, 10$ and when L is dynamically updated according to (5.1)–(5.2) at $T = 0.2$.

	Biot–Stokes alg.			Structure Darcy–Stokes alg.		
	e_F	$e_{\boldsymbol{\xi}}$	$e_{\boldsymbol{\eta}}$	e_F	$e_{\boldsymbol{\xi}}$	$e_{\boldsymbol{\eta}}$
$L = 0.1$	$1.102 \cdot 10^{-4}$	$2.216 \cdot 10^{-3}$	$4.745 \cdot 10^{-3}$	$1.108 \cdot 10^{-4}$	$2.332 \cdot 10^{-3}$	$4.691 \cdot 10^{-3}$
$L = 1$	$1.097 \cdot 10^{-4}$	$2.837 \cdot 10^{-3}$	$4.888 \cdot 10^{-3}$	$1.100 \cdot 10^{-4}$	$2.972 \cdot 10^{-3}$	$4.856 \cdot 10^{-3}$
$L = 10$	$1.101 \cdot 10^{-4}$	$2.904 \cdot 10^{-3}$	$4.906 \cdot 10^{-3}$	$1.106 \cdot 10^{-4}$	$2.881 \cdot 10^{-3}$	$4.795 \cdot 10^{-3}$
L_1	$1.088 \cdot 10^{-4}$	$1.836 \cdot 10^{-3}$	$4.683 \cdot 10^{-3}$	$1.098 \cdot 10^{-4}$	$1.795 \cdot 10^{-3}$	$4.564 \cdot 10^{-3}$
L_2	$1.092 \cdot 10^{-4}$	$1.796 \cdot 10^{-3}$	$4.682 \cdot 10^{-3}$	$1.102 \cdot 10^{-4}$	$1.771 \cdot 10^{-3}$	$4.568 \cdot 10^{-3}$
L_3	$1.093 \cdot 10^{-4}$	$1.794 \cdot 10^{-3}$	$4.696 \cdot 10^{-3}$	$1.103 \cdot 10^{-4}$	$1.789 \cdot 10^{-3}$	$4.588 \cdot 10^{-3}$

a smaller error is obtained for all the variables in both partitioned algorithms. In the case when (5.2) and (5.3) are used to update L, the error is smaller for all the variables when the Biot–Stokes algorithm is used. When the structure Darcy–Stokes scheme is used, the error is smaller for the solid velocity and displacement and only slightly larger than the smallest error obtained with a fixed L for the fluid velocity.

We note that in all the simulations performed in this example, no numerical instabilities were observed for the structure Darcy–Stokes algorithm, even though the purely elastic model for the structure was used.

5.3. Example 2. In the second example, we consider a benchmark problem describing flow from the fluid domain into a poroelastic medium. We assume that the fluid reference domain is $\hat{\Omega}_F = (0, 1) \times (0, 1)$ and that the structure reference domain is $\hat{\Omega}_P = (0, 1) \times (1, 1.5)$. At the left and right boundaries, we set $\boldsymbol{v} = 0, \boldsymbol{\eta} = 0$, and $\boldsymbol{q} \cdot \boldsymbol{n}_P = 0$. At the top structure boundary, we take $p_P = 0$ and set the poroelastic structure normal stress to zero. Finally, at the fluid bottom boundary, we prescribe $\boldsymbol{v} = (0, 4v_{in}x(1 - x))$, where $v_{in} = 5$.

To solve this problem, four different methods are considered. In particular, we use a monolithic method and the structure Darcy–Navier–Stokes method assuming that the fluid domain remains fixed and that the structure model is linear and given by (4.1) with $\mu_V = 0$. To investigate the impact of fixed versus moving domain assumption, we also solve the problem using the structure Darcy–Navier–Stokes method with the linear wall model, but assuming that the domain moves. Finally, to investigate the effect of the linear versus nonlinear structure model, we use the structure Darcy–Navier–Stokes method on a moving domain (Algorithm 3.2) with a compressible neo-Hookean hyperelastic wall model, given by [18]

$$\hat{\boldsymbol{W}} = C_1(\hat{I}_1 - tr(\boldsymbol{I}) - 2\ln \hat{J}) + D_1(\hat{J} - 1)^2, \tag{5.4}$$

where C_1 and D_1 are material constants, $\boldsymbol{I}$ is the identity matrix, and $\hat{I}_1 = tr(\hat{\boldsymbol{C}})$ is the first invariant of the right Cauchy–Green deformation tensor $\hat{\boldsymbol{C}}$. In all four cases considered here, the flow is modeled using the Navier–Stokes equations (2.2).

In this example, we use the Taylor–Hood elements, $\mathcal{P}_2$–$\mathcal{P}_1$, for the fluid velocity and pressure, $\mathcal{P}_2$ elements for the solid, and the Raviart–Thomas $\mathcal{RT}_1 - \mathcal{P}_1^{dc}$ elements [26] for the Darcy problem. The problem was solved with $\Delta x = 5 \cdot 10^{-2}$ and $\Delta t = 10^{-3}$, and the final time is $T = 3$ s. The parameters used in this problem are given in Table 2.

The combination parameter, L, was determined dynamically using (5.3), starting from L =2000. Newton's method is used for nonlinearities caused by the neo-Hookean

TABLE 2
The fluid and structure parameters used in Example 2.

Parameters	Values	Parameters	Values
Fluid density ρ_f (g/cm^3)	1	**Dynamic viscosity** μ (poise)	0.035
Wall density ρ_s(g/cm^3)	1.1	**Storativity coeff.** c_0 (cm^2/dyne)	10^{-3}
Shear modulus μ_P(dyne/cm^2)	1.67785×10^5	**Lamé's first par.** λ_P (dyne/cm^2)	$8.22148 \cdot 10^6$
Biot–Willis constant α	1	**Slip rate** γ (g/cm^2 s)	10^3
Fluid entry resist. δ (g/cm^2 s)	10		

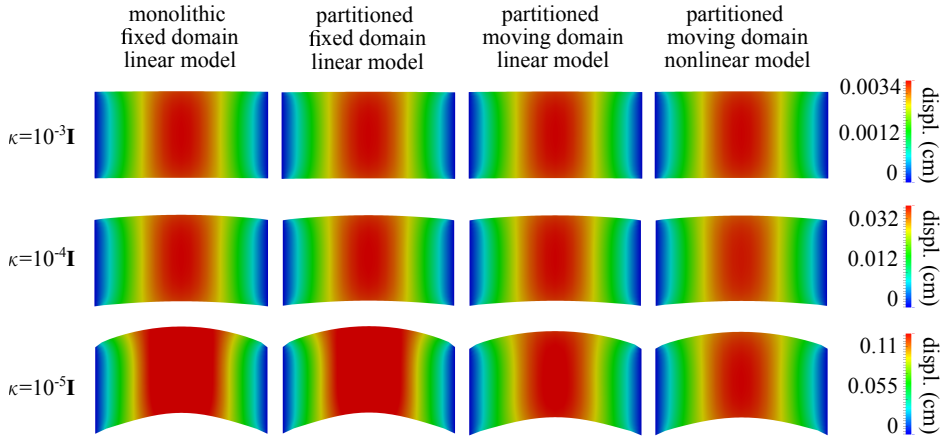

FIG. 5. *A comparison of the displacement obtained with* $\boldsymbol{\kappa} = 10^{-3}\boldsymbol{I}$ *(top),* $\boldsymbol{\kappa} = 10^{-4}\boldsymbol{I}$ *(middle), and* $\boldsymbol{\kappa} = 10^{-5}\boldsymbol{I}$ *cm^3 s/g (bottom) using four different methods, from left to right: a monolithic method with a fixed domain assumption and a linear wall model, the structure Darcy–Navier–Stokes method with a fixed domain assumption and a linear wall model, the structure Darcy–Navier–Stokes method with a moving domain assumption and a linear wall model, and the structure Darcy–Navier–Stokes method with a moving domain assumption and a nonlinear, hyperelastic wall model.*

wall model. We note that when $C_1 = \frac{\mu_P}{2}$ and $D_1 = \frac{\lambda_P}{2}$, which are the values used in this example, the neo-Hookean model is consistent with linear elasticity. In the following examples, we consider three different choices of the hydraulic conductivity tensor, $\boldsymbol{\kappa}$, i.e., $\boldsymbol{\kappa} = 10^{-3}\boldsymbol{I}, \boldsymbol{\kappa} = 10^{-4}\boldsymbol{I}$, and $\boldsymbol{\kappa} = 10^{-5}\boldsymbol{I}$ cm^3 s/g.

Figure 5 shows the poroelastic structure displacement obtained by four different methods considered in this example. Each domain is colored by the displacement magnitude and moved by the displacement vector for visualization purposes. The results obtained using $\boldsymbol{\kappa} = 10^{-3}\boldsymbol{I}$ are shown in the top row, the results obtained using $\boldsymbol{\kappa} = 10^{-4}\boldsymbol{I}$ are shown in the middle row, and the results obtained using $\boldsymbol{\kappa} = 10^{-5}\boldsymbol{I}$ are shown in the bottom row. Comparing the three rows, we can observe that the displacement increases when $\boldsymbol{\kappa}$ decreases. An excellent agreement is observed between the monolithic and the structure Darcy–Navier–Stokes method assuming a linear structural model and a fixed domain. When $\boldsymbol{\kappa} = 10^{-3}\boldsymbol{I}$ and $\boldsymbol{\kappa} = 10^{-4}\boldsymbol{I}$, all four methods give similar approximations. In the case when $\boldsymbol{\kappa} = 10^{-5}\boldsymbol{I}$, the displacement is relatively large, and the assumption that the domain is fixed gives results which overshoot the ones obtained using the moving domain assumption. We note that there are no large differences between the results obtained using a linear and a nonlinear wall model.

To further compare the displacements, we present the vertical displacement, η_y, over the line $y = 1.25$ in Figure 6. The left panel shows the results obtained using

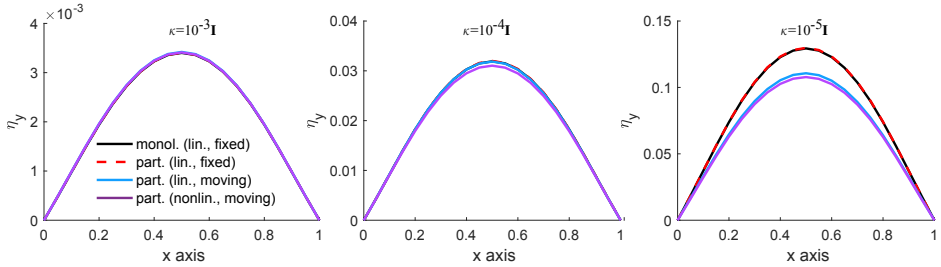

FIG. 6. *Vertical displacement, η_y, at $y = 1.25$ obtained with $\boldsymbol{\kappa} = 10^{-3}\boldsymbol{I}$ (left), $\boldsymbol{\kappa} = 10^{-4}\boldsymbol{I}$ (middle), and $\boldsymbol{\kappa} = 10^{-5}\boldsymbol{I}$ cm^3 s/g (right) using four different methods: a monolithic method with a fixed domain assumption and a linear wall model, the structure Darcy–Navier–Stokes method with a fixed domain assumption and a linear wall model, the structure Darcy–Navier–Stokes method with a moving domain assumption and a linear wall model, and the structure Darcy–Navier–Stokes method with a moving domain assumption and a nonlinear, hyperelastic wall model.*

$\boldsymbol{\kappa} = 10^{-3}\boldsymbol{I}$, the middle panel shows the results obtained using $\boldsymbol{\kappa} = 10^{-4}\boldsymbol{I}$, and the right panel shows the results obtained using $\boldsymbol{\kappa} = 10^{-5}\boldsymbol{I}$. When $\boldsymbol{\kappa} = 10^{-3}\boldsymbol{I}$, the displacements obtained using all four methods are roughly the same. A small difference between the linear and nonlinear wall model is observed when $\boldsymbol{\kappa} = 10^{-4}\boldsymbol{I}$. In this case, the moving domain assumption does not affect the solution. However, the nonlinear wall modes gives slightly smaller displacement than the linear wall model. When $\boldsymbol{\kappa} = 10^{-5}\boldsymbol{I}$, the most apparent difference is the one between the models that used the fixed domain assumption and those that used a moving domain assumption. In particular, when the problem is simplified and a fixed domain is used, the resulting displacements are significantly larger than the ones obtained using the moving domain assumption. While the linear and nonlinear wall models give similar approximations when the domain is moving, the displacement obtained using the non-linear model is slightly smaller than the displacement obtained using the linear wall model.

Finally, Figure 7 shows the fluid velocity in both domains obtained using $\boldsymbol{\kappa} = 10^{-3}\boldsymbol{I}$ (top) and $\boldsymbol{\kappa} = 10^{-5}\boldsymbol{I}$ (bottom). The velocities obtained using $\boldsymbol{\kappa} = 10^{-4}\boldsymbol{I}$ are very similar to the ones obtained using $\boldsymbol{\kappa} = 10^{-3}\boldsymbol{I}$ and therefore are not shown in the figure. As before, the same four methods are considered. The velocity is superimposed with the velocity magnitude. In both cases, an excellent agreement is observed between the monolithic method and the partitioned method when the domain is fixed and the structure model is linear. When $\boldsymbol{\kappa} = 10^{-5}\boldsymbol{I}$, a significant difference can be seen between the cases when a fixed domain assumption is used versus the moving domain cases. We observe that more flow enters the poroelastic domain when the domain is allowed to deform.

6. Conclusions. This work focuses on the numerical modeling of the FPSI problem with large structural displacements. In particular, we considered the coupled problem where the flow is described using the Navier–Stokes equations in the ALE form and the structure is described using the Biot model. We used the dual-mixed formulation of the Darcy equations and a hyperelastic structural model. We introduced two novel numerical methods based on the Robin–Robin interface conditions, which were obtained by multiplying the kinematic coupling condition by a combination parameter, L, and adding it to the dynamic condition describing the momentum conservation in the fluid phase. In the first proposed method (Algorithm 3.1), the Biot problem is solved separately from the fluid problem, while in the second proposed method (Algorithm 3.2) the Biot problem is additionally split into a mechanics

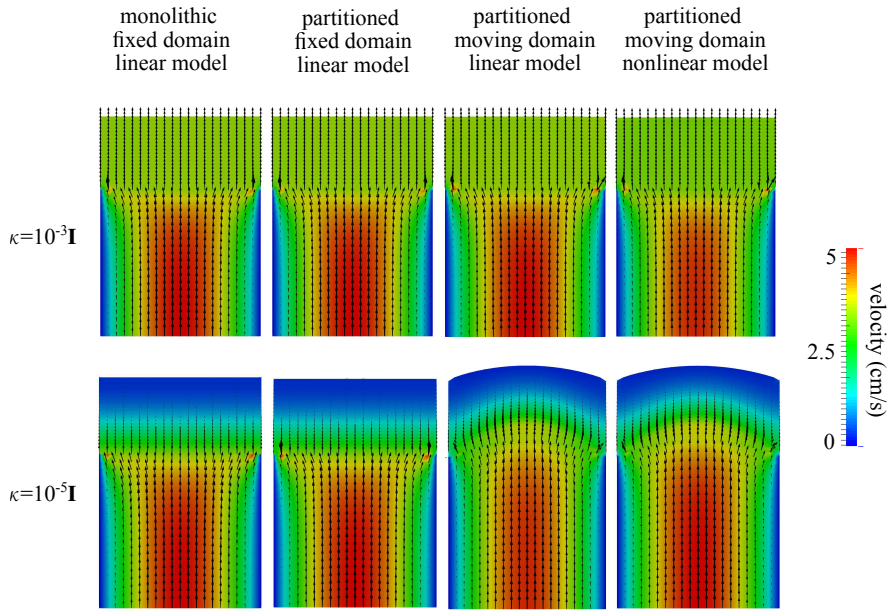

FIG. 7. *A comparison of the fluid and Darcy velocities obtained with* $\boldsymbol{\kappa} = 10^{-3}\boldsymbol{I}$ *(top) and* $\boldsymbol{\kappa} = 10^{-5}\boldsymbol{I}$ cm^3 s/g *(bottom) using four different methods, from left to right: a monolithic method with a fixed domain assumption and a linear wall model, the structure Darcy–Navier–Stokes method with a fixed domain assumption and a linear wall model, the structure Darcy–Navier–Stokes method with a moving domain assumption and a linear wall model and the structure Darcy–Navier–Stokes method with a moving domain assumption and a nonlinear, hyperelastic wall model.*

problem and a Darcy problem. In that way, we can solve the mechanics problem first in the Lagrangian formulation, compute the new domain, and then solve the Darcy and the Navier–Stokes problems in the deformed domain.

We presented the stability analysis of the proposed methods on a simplified problem and showed that Algorithm 3.1 is unconditionally stable and that Algorithm 3.2 is stable when the structure is viscoelastic and when the problem parameters and the time step satisfy conditions (4.7). However, in the numerical examples considered in this manuscript, no stability issues were seen even when the structure was purely elastic.

Our first example shows a first-order convergence in time when the values of L are sufficiently large on a simplified example where the structure is assumed to be linear and the fluid domain remains fixed. In the same example, a dynamic update of L is suggested, which keeps the errors in the approximation of the kinematic and dynamic coupling conditions of a similar size. Our results indicate that the proposed dynamic update of L yields similar or smaller errors when compared across different, fixed choices of L.

In the second numerical example, we investigated the effects of linear assumptions in both the structural wall model, and the fluid-poroelastic structure coupling, where the fluid domain is assumed to be fixed. In the example considered in this study, the results obtained using the fixed versus the moving domain model increasingly differ as the displacements increase. A smaller discrepancy is observed between the linear and non-linear, hyperelastic wall models when the moving domain problem was considered in both cases. The results obtained using a linear wall model and a fixed

domain were compared to the ones obtained using a monolithic scheme with the same assumptions, showing an excellent agreement. Hence, our results indicate that if the physics of the problem is such that the displacement of the poroelastic medium is significant, a moving domain model would need to be considered in order to obtain a more accurate approximation. While we did not observe a large difference between the results obtained using the linear versus nonlinear wall model, we would expect the difference to become more apparent for problems with larger displacements.

The drawback of this work is that the analysis is performed on a simplified problem and that only two-dimensional examples are presented. However, the same methodology could be applied to three-dimensional problems. While we did not observe instabilities even though $\mu_V = 0$ was used in both examples, if the instabilities occur, (4.17) could be used to provide an upper bound on the dynamic estimate of L. Alternatively, Algorithm 3.1 could be applied, for which we do not have any stability conditions when analyzed in a simplified, linearized form.

Appendix A. Inequalities used in the stability analysis.

LEMMA A.1. *Suppose $S \subset \mathbb{R}^d$ is an open set with piecewise smooth boundary and Γ is part of ∂S with positive measure. The following inequalities hold true:*

Young's inequality:

$$ab \leq \frac{a^2}{2\epsilon} + \frac{\epsilon b^2}{2} \quad \text{for nonnegative real numbers } a, b \text{ and } \epsilon > 0; \tag{A.1}$$

the Cauchy–Schwarz inequality:

$$\left| \int_S \boldsymbol{v} \cdot \boldsymbol{u} d\boldsymbol{x} \right| \leq ||\boldsymbol{v}||_{L^2(S)} ||\boldsymbol{u}||_{L^2(S)} \quad \forall \boldsymbol{v}, \boldsymbol{u} \in L^2(S); \tag{A.2}$$

the Poincaré–Friedrichs inequality: assuming that $\boldsymbol{v} \in (H^1(S))^d$ vanishes on a part of the boundary ∂S with positive measure, there exists a positive constant C_P depending on S such that

$$||\boldsymbol{v}||_{L^2(S)} \leq C_P ||\nabla \boldsymbol{v}||_{L^2(S)}; \tag{A.3}$$

the trace inequality: there exists a constant $C_T > 0$ depending on S such that

$$||\boldsymbol{v}||_{L^2(\Gamma)} \leq C_{tr} ||\boldsymbol{v}||^{1/2}_{L^2(S)} ||\nabla \boldsymbol{v}||^{1/2}_{L^2(S)} \quad \forall \boldsymbol{v} \in H^1(S); \tag{A.4}$$

Korn's inequality: assuming that $\boldsymbol{v} \in (H^1(S))^d$ vanishes on a part of the boundary ∂S with positive measure, there exists a positive constant C_K depending on S such that

$$||\nabla \boldsymbol{v}||_{L^2(S)} \leq C_K ||\boldsymbol{D}(\boldsymbol{v})||_{L^2(S)}. \tag{A.5}$$

REFERENCES

[1] I. AMBARTSUMYAN, V. J. ERVIN, T. NGUYEN, AND I. YOTOV, *A nonlinear Stokes–Biot model for the interaction of a non-newtonian fluid with poroelastic media*, ESAIM Math. Model. Numer. Anal., 53 (2019), pp. 1915–1955.

[2] I. AMBARTSUMYAN, E. KHATTATOV, I. YOTOV, AND P. ZUNINO, *A Lagrange multiplier method for a Stokes–Biot fluid–poroelastic structure interaction model*, Numer. Math., 140 (2018), pp. 1–41.

[3] D. N. ARNOLD, F. BREZZI, AND M. FORTIN, *A stable finite element for the Stokes equations*, Calcolo, 21 (1984), pp. 337–344.

[4] S. Badia, A. Quaini, and A. Quarteroni, *Coupling Biot and Navier–Stokes equations for modelling fluid–poroelastic media interaction*, J. Comput. Phys., 228 (2009), pp. 7986–8014.
[5] S. Basting, A. Quaini, S. Čanić, and R. Glowinski, *Extended ALE method for fluid–structure interaction problems with large structural displacements*, J. Comput. Phys., 331 (2017), pp. 312–336.
[6] E. Bergkamp, C. Verhoosel, J. Remmers, and D. Smeulders, *A staggered finite element procedure for the coupled Stokes–Biot system with fluid entry resistance*, Comput. Geosci., 24 (2020), pp. 1497–1522.
[7] M. A. Biot, *Theory of deformation of a porous viscoelastic anisotropic solid*, J. Appl. Phys., 27 (1956), pp. 459–467.
[8] M. Bukač, *A loosely-coupled scheme for the interaction between a fluid, elastic structure and poroelastic material*, J. Comput. Phys., 313 (2016), pp. 377–399.
[9] M. Bukač, I. Yotov, R. Zakerzadeh, and P. Zunino, *Partitioning strategies for the interaction of a fluid with a poroelastic material based on a Nitsche's coupling approach*, Comput. Methods Appl. Mech. Engrg., 292 (2015), pp. 138–170.
[10] M. Bukač, I. Yotov, and P. Zunino, *An operator splitting approach for the interaction between a fluid and a multilayered poroelastic structure*, Numer. Methods Partial Differential Equations, 31 (2015), pp. 1054–1100.
[11] M. Bukač, I. Yotov, and P. Zunino, *Dimensional model reduction for flow through fractures in poroelastic media*, ESAIM Math. Model. Numer. Anal., 51 (2017), pp. 1429–1471.
[12] E. Burman and M. Fernández, *Stabilization of explicit coupling in fluid-structure interaction involving fluid incompressibility*, Comput. Methods Appl. Mech. Engrg., 198 (2009), pp. 766–784.
[13] J. Chen, *Time domain fundamental solution to Biot's complete equations of dynamic poroelasticity. Part* I*: Two-dimensional solution*, Int. J. Solids Structures, 31 (1994), pp. 1447–1490.
[14] M. Discacciati, A. Quarteroni, and A. Valli, *Robin–robin domain decomposition methods for the Stokes–Darcy coupling*, SIAM J. Numer. Anal., 45 (2007), pp. 1246–1268.
[15] J. Donea, *Arbitrary Lagrangian–Eulerian finite element methods*, in Computational Methods for Transient Analysis, North-Holland, Amsterdam, 1983.
[16] L. Formaggia, A. Quarteroni, and A. Veneziani, *Cardiovascular Mathematics: Modeling and Simulation of the Circulatory System*, vol. 1, Springer Science & Business Media, New York, 2010.
[17] F. Hecht, *New development in FreeFem++*, J. Numer. Math., 20 (2012), pp. 251–265.
[18] C. O. Horgan and G. Saccomandi, *Constitutive models for compressible nonlinearly elastic materials with limiting chain extensibility*, J. Elasticity, 77 (2004), pp. 123–138.
[19] T. Hughes, W. Liu, and T. Zimmermann, *Lagrangian–Eulerian finite element formulation for incompressible viscous flows*, Comput. Methods Appl. Mech. Engrg., 29 (1981), pp. 329–349.
[20] N. Koshiba, J. Ando, X. Chen, and T. Hisada, *Multiphysics simulation of blood flow and LDL transport in a porohyperelastic arterial wall model*, J. Biomech. Engrg., 129 (2007), pp. 374–385.
[21] P. Le Tallec, J.-F. Gerbeau, P. Hauret, and M. Vidrascu, *Fluid structure interaction problems in large deformation*, C. R. Mec., 333 (2005), pp. 910–922.
[22] T. Li and I. Yotov, *A Mixed Elasticity Formulation for Fluid-Poroelastic Structure Interaction*, arXiv preprint, arXiv:2011.00132 [math.NA], 2020.
[23] F. Nobile, *Numerical Approximation of Fluid-Structure Interaction Problems with Application to Haemodynamics*, PhD thesis, EPFL, Switzerland, 2001.
[24] O. Oyekole and M. Bukač, *Second-order, loosely coupled methods for fluid-poroelastic material interaction*, Numer. Methods Partial Differential Equations, 36 (2020), pp. 800–822.
[25] A. D. Rauch, A.-T. Vuong, L. Yoshihara, and W. A. Wall, *A coupled approach for fluid saturated poroelastic media and immersed solids for modeling cell-tissue interactions*, Int. J. Numer. Methods Biomed. Eng., 34 (2018), p. e3139.
[26] P.-A. Raviart and J.-M. Thomas, *A mixed finite element method for* 2*-nd order elliptic problems*, in Mathematical Aspects of Finite Element Methods, Springer, Cham, 1977, pp. 292–315.
[27] A. P. Selvadurai, *Mechanics of Poroelastic Media*, Springer Science & Business Media, New York, 2013.
[28] R. E. Showalter, *Poroelastic filtration coupled to Stokes flow*, in Control Theory of Partial Differential Equations, G. Leugering, O. Imanuvilov, B.-Y. Zhang, and R. Triggiani, eds., Chapman and Hall/CRC, Boca Raton, FL, 2005.

[29] R. Zakerzadeh, *A Computational Model for Fluid-Porous Structure Interaction*, PhD thesis, University of Pittsburgh, 2016.
[30] R. Zakerzadeh and P. Zunino, *A computational framework for fluid–porous structure interaction with large structural deformation*, Meccanica, 54 (2019), pp. 101–121.